CHARACTERIZING THE SEPARATION AND REATTACHMENT OF SUCTION SURFACE BOUNDARY LAYER IN LOW PRESSURE TURBINE USING MASSIVELY PARALLEL LARGE EDDY SIMULATIONS

A Thesis

by

SHRIRAM JAGANNATHAN

Submitted to the Office of Graduate Studies of
Texas A&M University
in partial fulfillment of the requirements for the degree of

MASTER OF SCIENCE

December 2010

Major Subject: Mechanical Engineering

CHARACTERIZING THE SEPARATION AND REATTACHMENT OF SUCTION SURFACE BOUNDARY LAYER IN LOW PRESSURE TURBINE USING MASSIVELY PARALLEL LARGE EDDY SIMULATIONS

A Thesis

by

SHRIRAM JAGANNATHAN

Submitted to the Office of Graduate Studies of
Texas A&M University
in partial fulfillment of the requirements for the degree of

MASTER OF SCIENCE

Approved by:

Co-Chairs of Committee,	Andrew Duggleby
	Taher Schobeiri
Committee Members,	Hamn-Ching Chen
Head of Department,	Dennis O'Neal

December 2010

Major Subject: Mechanical Engineering

ABSTRACT

Characterizing the Separation and Reattachment of

Suction Surface Boundary Layer in Low Pressure Turbine

Using Massively Parallel Large Eddy Simulations. (December 2010)

Shriram Jagannathan, B.Tech., National Institute of Technology, Tiruchirappalli

Co–Chairs of Advisory Committee: Dr.Andrew Duggleby
Dr.Taher Schobeiri

The separation and reattachment of the suction surface boundary layer in a low pressure turbine is characterized using large-eddy simulation at Re=68,000 based on freestream velocity and suction surface length. A high pass filtered Smagorinsky model is used for modeling the sub-grid scales. The onset of time mean separation is at $s/s_o = 0.61$ and reattachment at $s/s_o = 0.81$, extending over 20% of the suction surface. The boundary layer is convectively unstable with a maximum reverse flow velocity of about 13% of freestream. The breakdown to turbulence occurs over a very short distance of suction surface which is followed by reattachment. Detailed investigations into the structure and kinematics of the bubble and turbulence statistics are presented. The vortex shed from the bubble, convects downstream and interacts with the trailing edge vortices increasing the turbulence intensity. On the suction side, dominant hairpin structures near the transitional and turbulent flow regime are observed. These hairpin vortices are carried by the freestream even downstream of the trailing edge of the blade with a possibility of reaching the next stage. Longitudinal streaks that evolve from the breakdown of hairpin vortices formed near the leading edge are observed on the pressure surface.

To my parents and sister

ACKNOWLEDGMENTS

First, I would like to thank my advisor, Andrew Duggleby, for his guidance, patience and support during the course of my thesis. I shall also like to thank Taher Schobeiri for generously sharing the experimental data. My sincere thanks to Paul Fischer for his valuable suggestions. I am pleased to thank Markus Schwänen for his help during my stint at FT^2L, be it Latex, Linux, turbomachinery or CFD, he has always lent a helping hand. My special thanks to former and present cheerful members of FT^2L: Yuval Doron (UV), Pradeep Rao, Michael Meador, Sebastian J. Eluvathingal, Josh Camp and William Pollard for their support.

NOMENCLATURE

C	Chord
C_p	Pressure coefficient, $\frac{p - p_\infty}{\frac{1}{2}\rho U_\infty^2}$
C_{ax}	Axial chord
H_{12}	Form factor
R_{11}	Correlation coefficient
Tu	Turbulence intensity
U_e	Boundary layer edge velocity
U_∞	Freestream velocity
δ_1	Displacement thickness of a boundary layer
δ_2	Momentum thickness of a boundary layer
λ	Eigenvalue
Re	Reynolds number based on suction surface length and freestream velocity
Re_θ	Reynolds number based on momentum thickness at separation and boundary layer edge velocity
rms	root-mean-square
$\overline{\Delta}$	Filter width
ρ	Density

l	Bubble length
s	Surface coordinate
s_o	Suction or pressure surface length
DNS	Direct Numerical Simulation
FSTI	Freestream Turbulence Intensity
HPF	High Pass Filter
LES	Large Eddy Simulation
LPT	Low Pressure Turbine
RANS	Reynolds Averaged Navier Stokes Equation

TABLE OF CONTENTS

CHAPTER Page

LIST OF TABLES

LIST OF FIGURES

FIGURE Page

FIGURE Page

FIGURE Page

FIGURE Page

FIGURE Page

FIGURE Page

CHAPTER I

INTRODUCTION AND LITERATURE REVIEW

A. Introduction

Technological advancements in the past few decades led to the discovery of jet aircraft, the fastest means of transportation. The speed of a typical commercial aircraft, Boeing 747, is about 550mph. The aircraft needs to generate enormous power to fly at such high speeds and to carry the passengers. This power is generated from an engine known as gas turbine engine since it uses air as a medium to transport the power generated. Gas turbines also finds its application in power generation where electricity is generated. But, the gas turbine engine imposes enough scientific complications that a small improvement could eventually lead to a savings of millions of dollars for the industries. The complication is primarily due to the presence of innumerable parts that constitute the engine. One of the broad challenges concerning engineers is increasing the efficiency of the engine.

In simplistic terms, any machine with a rotating component converting energy from one type to another can be classified as turbomachines [1]. In turbomachinery literature, devices that convert kinetic energy into potential energy are classified as *pumps*. *Turbines* work the other way, converting potential to kinetic energy. The present study addresses an issue, flow separation, that grossly affects the efficiency of gas turbine when left uncontrolled.

The journal model is *IEEE Transactions on Automatic Control.*

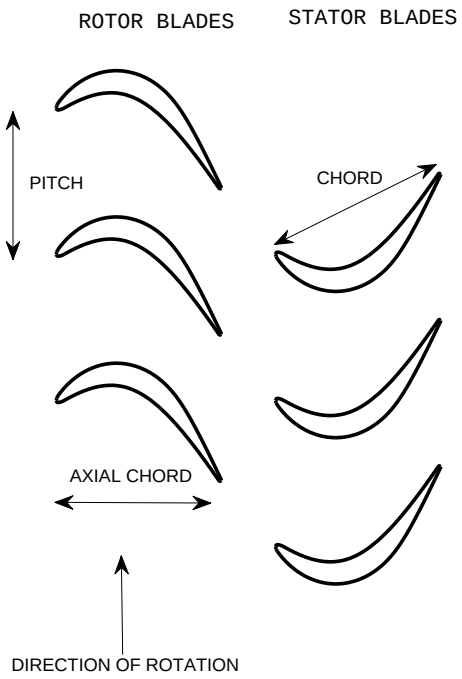

Fig. 1. The figure shows the rotor and stator blades in a turbine stage. The blade cascade is circular in a gas turbine, but for simplicity it is shown linear. The terminologies of pitch, axial chord and chord used in the forthcoming sections are shown figuratively.

1. Gas Turbines

a. Terminologies

In turbomachinery, any set of rotating blades are called as *rotors* and stationary blades are known as *stators*. Stators and rotors together constitute a *stage*. Fig. 1 shows a schematic diagram of a stage and also indicates the direction of rotation of the rotor. A number of stator and rotor blades are mounted on a circular cross-sectional shaft called *hub* that extends throughout the gas turbine. The purpose of rotor is to add adequate amount of energy (rotational energy) to the working fluid while the stators

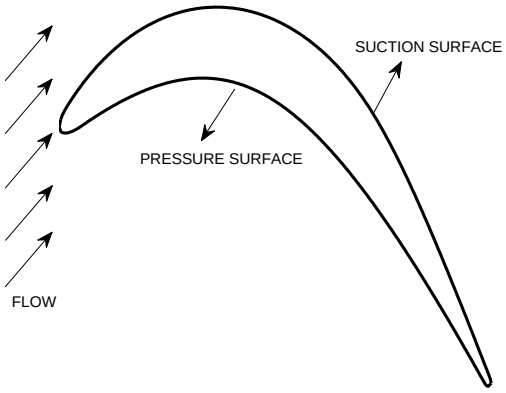

Fig. 2. Blade nomenclature: The convex surface is called suction surface since it has lesser pressure than the corresponding concave pressure side. The flow hits the blade at an angle to the horizontal known as *angle of attack*.

simply divert the flow to the next rotor [2]. Each of these blades (rotor or stator) take different shapes according to the application, for example, compressor blades are flat and thin while turbine blades have higher radius of curvature and tend to be thicker than the compressor blades. Fig. 2 shows a turbine blade with the nomenclature of suction and pressure surface that is used in the present study and literature. The convex side of a blade is referred to as suction surface and concave side as pressure surface. This is because the pressure on the suction side is significantly lesser than that of the pressure surface.

b. Operation

Gas turbines are widely used in aviation industry since it has a higher thrust to weight ratio. A simple gas turbine engine consists of an inlet nozzle, a compressor, combustion chamber, a turbine and an exit diffuser. The atmospheric air enters

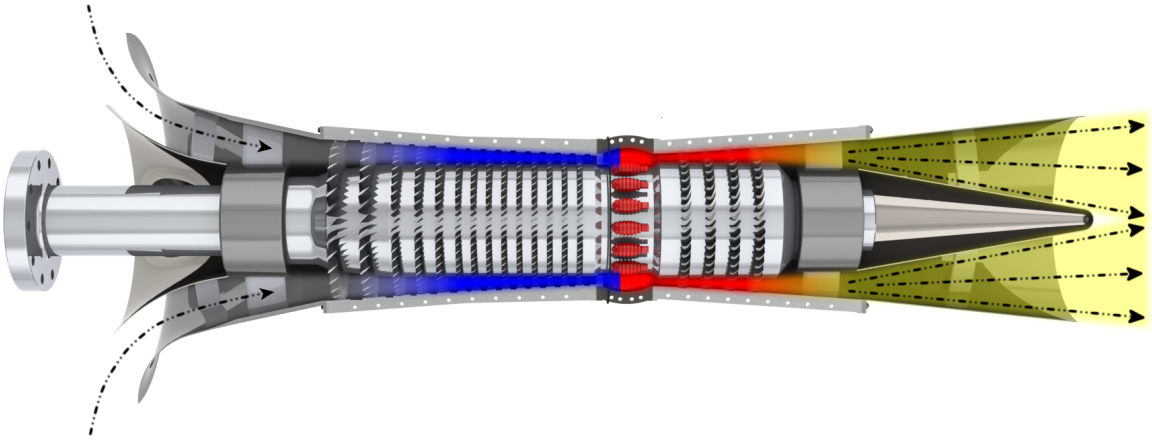

Fig. 3. Section view of a gas turbine engine with only the rotors. The stators are attached to the casing of the gas turbine and sits in between the rotors. The path of fluid from inlet nozzle and its subsequent movement till the diffuser is shown. As it passes through the compressor, the temperature and pressure rises, while it reduces during the expansion process in the turbine and further in the diffuser. The colors blue, yellow and red qualitatively represent low, medium and high values. Image taken from the author's MEEN 646-Class Project.

the nozzle and is compressed as it passes over the compressor. The compression is achieved though addition of rotational energy in the rotor that leads to a pressure rise across each stage [2]. The compressed air is injected into the combustion chamber where it mixes with the fuel and ignites. This produces enormous amount of energy, part of which drives the turbine rotors. The process is shown schematically in Fig. 3 and Fig. 4. Based on the positioning, gas turbine stages could further be classified as low, intermediate and high pressure compressors and turbines. The low pressure components are usually positioned near the inlet and exit of gas turbine since the operating conditions are close to atmospheric.

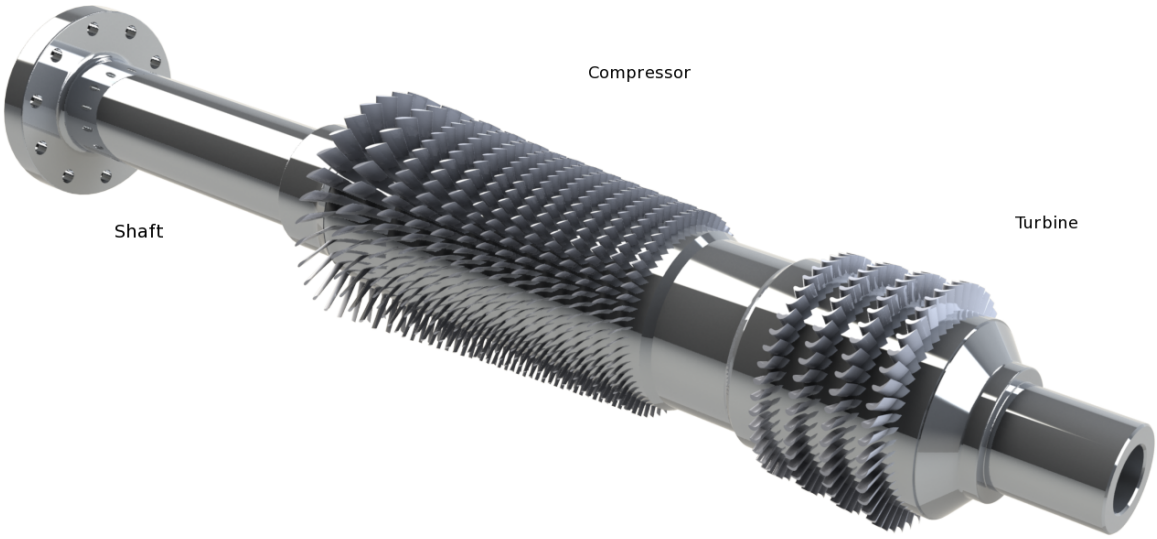

Fig. 4. The figure shows the shaft that connects the compressor and turbine with the rotor blades mounted on it. The combustion chamber that is placed in between the compressor and turbine is not shown in this picture. Image taken from the author's MEEN 646-Class Project.

c. Thermodynamics

Since a stage consists of rotating and stationary blades, it is necessary to define stationary and relative frame of reference for deducing the energy balance in turbomachines. Absolute velocities are denoted by $\mathbf{V}$, relative velocity $\mathbf{W}$ and rotational velocity of rotors $\mathbf{U}$ with subscripts $1, 2, 3$ describing stator inlet, rotor inlet and rotor exit in Fig. 5. The fluid enters the stator and gets deflected with an increase in kinetic energy. The total enthalpy, which is a sum of static enthalpy and enthalpy due to the kinetic energy of the fluid, is constant in both stator and rotor (in rotational frame of reference) due to conservation of energy. From the first law of thermodynamics, the difference in total enthalpy between the stages is the internal energy of the fluid ($\mathbf{H_1} - \mathbf{H_3}$). This is the work done per stage and is denoted as $\mathbf{l_m}$ in Fig. 5.

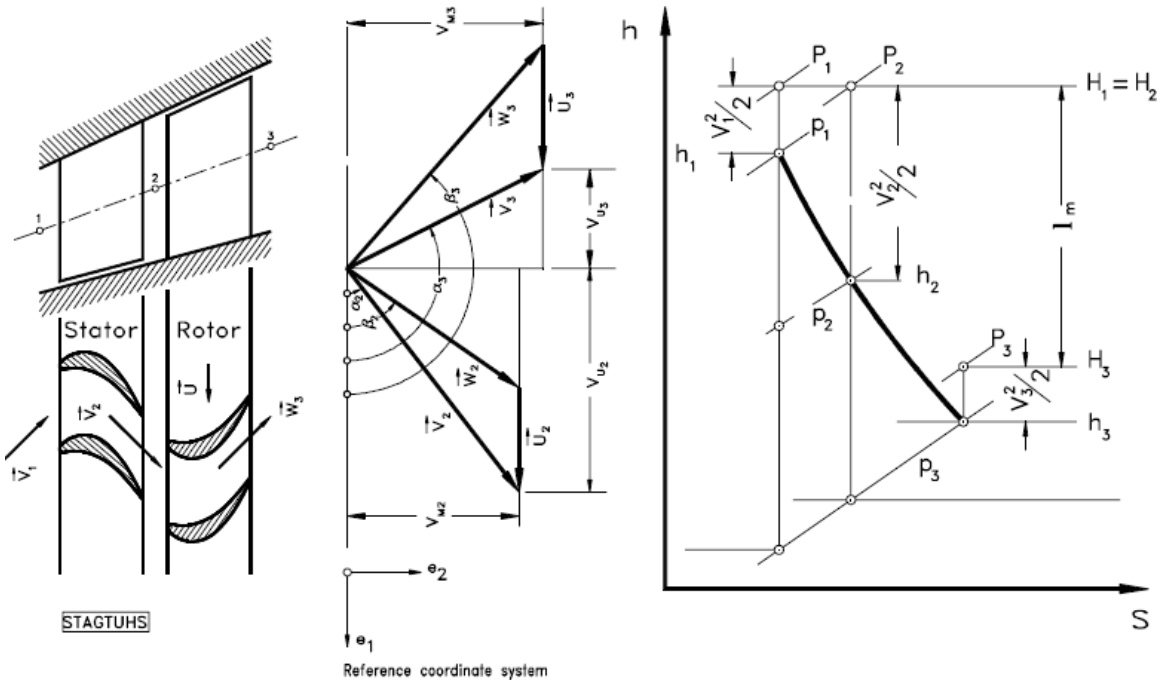

Fig. 5. Thermodynamic process in a turbine stage, taken from Schobeiri [2]. The fluid enters the stator and gets deflected with an increase in kinetic energy that is shown in the velocity triangle and the h-s diagram. The total enthalpy in constant in stator and rotor(in rotational frame of reference) which is shown as $\mathbf{H_1 = H_2}$. In absolute frame of reference the difference in total enthalpy between the stages is the work done per stage and is denoted as $\mathbf{l_m}$ in the figure.

2. Computational Fluid Dynamics

Fluid flow exist naturally, for example, stirring motion in a cup of coffee, dripping of honey, blood flow, smoke from a chimney etc all represent a type of flow encountered in daily life. However unrelated these flows may seem, they could all be characterized with one parameter, Reynolds Number. Osborne Reynolds [3] in his seminal paper, discovered that the ratio of inertial forces to viscous force, Reynolds Number(Re), could determine the characteristics of any flow. Based on the Re, flows could be

classified as laminar, turbulent and transitional (that are intermittent to both). The difference between laminar and turbulent flow is the inherent mixing of adjacent fluid layers in turbulent flows [4]. Laminar flows tend to be smooth without any mixing between the fluid layers while turbulent flows exhibit mixing in macroscopic scales [4].

The flows mentioned above could be driven by external means like pressure gradient or gravity. Pressure gradient is the rate of change of pressure with distance and is termed *favorable* if the flow is along direction of decreasing pressure (negative pressure gradient). On the contrary, pressure gradient is *adverse* if the flow is in the direction of increasing pressure (positive pressure gradient). Here, the pressure gradient resists the flow and if the net pressure force acts opposite to the direction of flow, the fluid will separate from the surface [4]. This is because the kinetic energy of the fluid close to the surface is very less and hence the boundary layer is very susceptible to separation. The other resistance to a fluid flow is its viscosity. Viscous effects are usually felt within a region close to the surface known as *boundary layer*.

Computational Fluid Dynamics (CFD) is a branch of fluid dynamics that deal with study of fluid flow by solving the equations of motion (to be discussed in SectionC) using computers. Often experimental and computational analysis are performed in conjunction to increase the level of confidence in the results achieved. CFD is advantageous over experiments when experimental measurement and analysis becomes exceedingly difficult. For example, experimentally it is practically impossible to describe the flow field in a gas turbine engine at all spatial locations and time instances, but large scale computations can be performed over the entire gas turbine to describe the flow-field. In any CFD simulation, the geometry is first divided into a finite number of elements which are further sub-divided into a number of nodes. The equations of motion are discretized and solved, for velocities and pressure, on each node and at each time instant. This gives access to data at any user-defined location

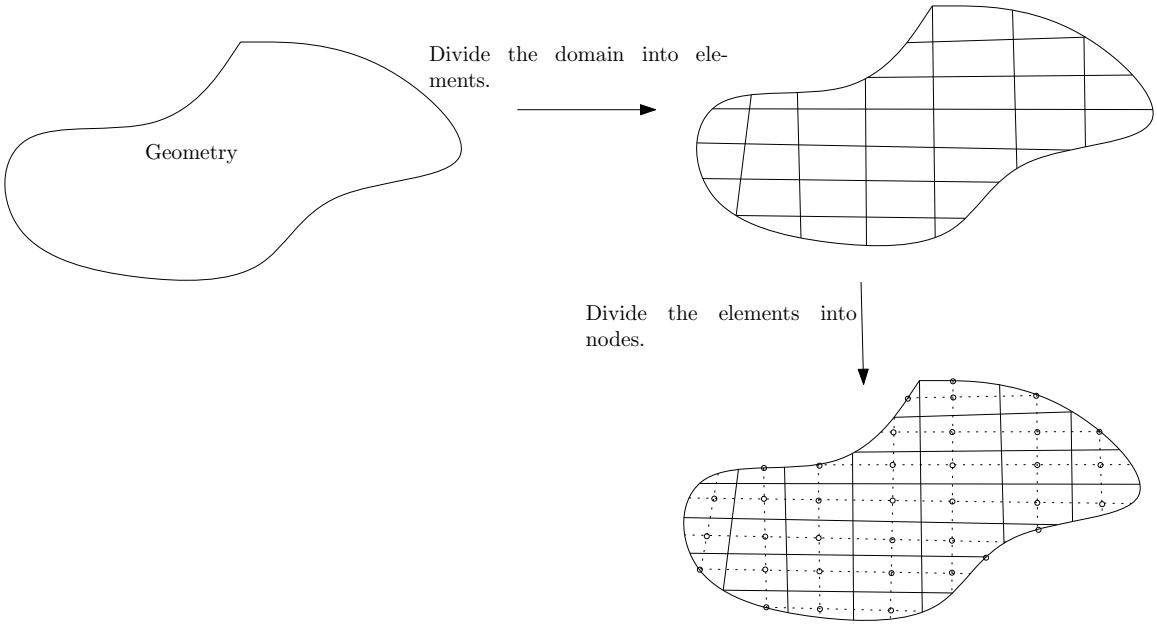

Fig. 6. The figure shows sequence of steps prior to a CFD simulation. The domain is divided into discrete elements which are then sub-divided into nodes. The circles represent the nodes interior of each element. The adjoining vertices of each element are also nodes but are not shown here. The velocities and pressure are known at all the nodes after the computation.

and time instant. Fig. 6 gives a schematic representation of the process.

B. Problem Statement

Due to the angle of attack and the high curvature associated with low pressure turbines, they are subjected to adverse pressure gradients. This can lead to separation of the boundary layer on the suction surface if the adverse pressure gradient is strong enough to overcome the momentum carried by the fluid [5]. At certain Reynolds number the flow reattaches on the suction side forming a separation bubble as shown in Fig. 7. Upon separation, the boundary layer grows in size increasing the drag on the blade, until it becomes turbulent and reattaches [6]. In aircraft engines, the above said

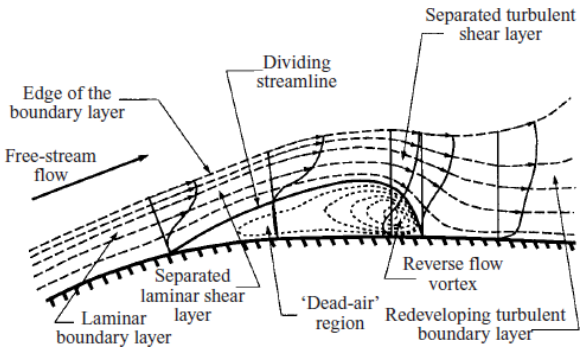

Fig. 7. Mean dividing streamline of separation bubble taken from Horton [7]. The figure shows the velocity profiles prior and aft-separation near the bubble. The point of zero velocity gradient at the wall gives the reattachment point. The recirculation zone inside the bubble is shown as dead-air region.

phenomenon occur at cruise condition when the Reynolds number is 50,000-250,000 [8]. So, its imperative that the dynamics of separation be predicted accurately for its active control. Also, separation inhibits pressure recovery and this difference in pressure, increases the pressure drag on the blade. The present study focuses on quantifying the onset and reattachment of separation, effect of freestream disturbances on the separation bubble, the type of transition associated with the reattachment, characterizing the flow structure due to the bubble and the vortex dynamics downstream of the reattachment region.

Flows in turbomachinery components are complex due to the intricate internal geometry of the passages, separation and reattachment of the boundary layer, secondary flows, interaction of upstream wakes with boundary layer among many others. Often times the 3-dimensional nature of the flow structure and dynamics in separation and transition makes the data experimentally inaccessible. Further, boundary layer measurements in experiments are challenging due to the extremely small size of boundary layer. It is also difficult to visualize experimentally the instantaneous

separation and reattachment of the boundary layer, the vortices shed downstream of the reattachment region and the instability that triggers the transition. These high complexities are a natural environment for accurate, time-resolved CFD to make a substantial impact in the understanding of the underlying physics involved

C. Computational Preliminaries

The Navier-Stokes equation and equation of continuity is given by,

$$\frac{\partial U_i}{\partial t} + \frac{\partial}{\partial x_j}\left(U_i U_j\right) = -\frac{1}{\rho}\frac{\partial p}{\partial x_i} + \nu\frac{\partial}{\partial x_j}\left(\frac{\partial U_i}{\partial x_j} + \frac{\partial U_j}{\partial x_i}\right), \tag{1.1}$$

$$\frac{\partial U_i}{\partial x_i} = 0. \tag{1.2}$$

Eqn.(1.1) represents conservation of momentum in all the spatial directions ($i = 1, 2, 3$) and Eqn.(1.2) is from conservation of mass, often known as incompressibility condition. Here, U is the velocity, p pressure, ν kinematic viscosity and ρ density. The second term on the left side in Eqn.(1.1) denotes the non-linear interaction in the flow, while the terms on the right side are sum of pressure and viscous forces. Theoretically, Navier-Stokes equation is applicable to all types of flow (laminar,turbulent and transitional) and is capable of predicting all the scales of motion. However, to accurately resolve all the scale requires extensive computational resources that limits its application only to low Re flows. This type of simulation is called *Direct Numerical Simulation* where all the scales are solved numerically without any models. But for applications wherein only the mean flow is of interest, the Navier-Stokes equation is averaged by splitting the exact solution into a mean and fluctuating part and then numerically solved. This is called as Reynolds Averaged Navier-Stokes (RANS). RANS approach suffers from many deficiencies when applied to flows that

are transitional in nature. The assumption that the scales of motion are uniform in all directions(isotropic) does not hold true in transitional flows or when the flow accelerates. The incapacity of RANS to predict instantaneous flow phenomenon like transition could also be attributed to the assumption that the mean flow is steady.

Mathematically the RANS equations are expressed as,

$$q_i = \bar{Q}_i + q_i, \quad \text{where q is } u, v, w \text{ or } p. \tag{1.3a}$$

$$\frac{\partial \bar{U}_i}{\partial x_i} = 0, \frac{\partial u_i}{\partial x_i} = 0, \tag{1.3b}$$

$$\frac{\partial \bar{U}_i}{\partial t} + \bar{U}_j \frac{\partial \bar{U}_i}{\partial x_j} = -\frac{1}{\rho}\frac{\partial \bar{p}}{\partial x_i} + \nu \frac{\partial^2 \bar{U}_i}{\partial^2 x_j} - \frac{\partial \overline{u_i u_j}}{\partial x_j} \quad . \tag{1.3c}$$

Since only mean quantities are computed, the fluctuating term ($\overline{u_i u_j}$) known as *Reynolds stress* is modeled with an assumption:

$$-\overline{u_i u_j} = 2\nu_t S_{ij} - \frac{2}{3} k \delta_{ij}, \tag{1.4}$$

where S_{ij} is the mean rate of strain defined by Eqn. 1.5.

$$S_{ij} = \frac{1}{2}\left(\frac{\partial \bar{U}_i}{\partial x_j} + \frac{\partial \bar{U}_j}{\partial x_i}\right) \tag{1.5}$$

1. Introduction to Large Eddy Simulation

Large Eddy Simulation is based on Richardson's assumption [9] of identifying large and small eddies in a fluid flow. According to Pope [10], an eddy is perceived as a turbulent motion localized within a region of size l that is moderately coherent over the region. The large eddies are unstable and break into small eddies which further evolve as smaller eddies [10], transferring energy in each process. This continuous transfer of energy from large eddies to small eddies is known as energy cascade. The cascading process continues until the eddies are stable where viscous dissipation takes

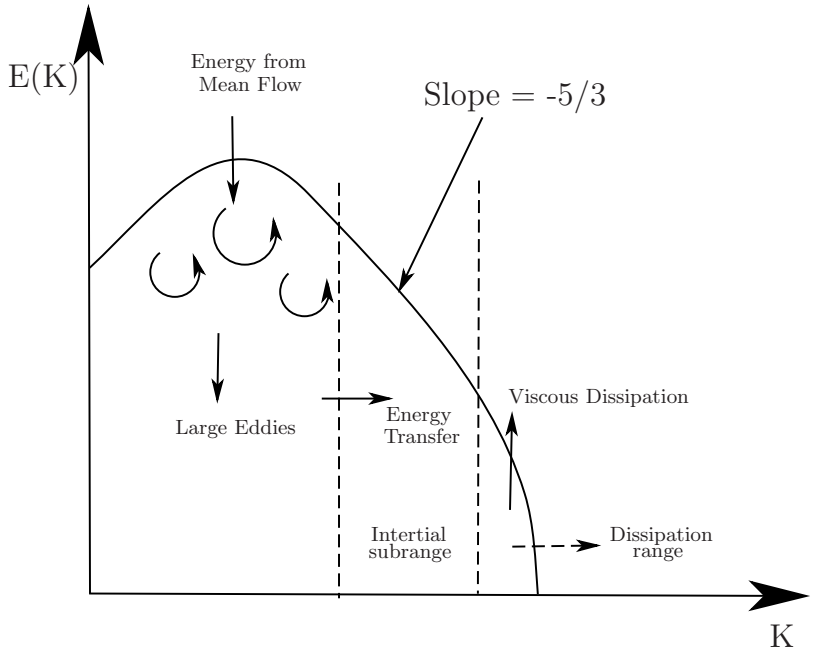

Fig. 8. Energy Spectrum showing the different range of motion in a turbulent flow [11]. The energy is cascaded from large scales to small scales and further till viscosity takes over.

over. Fig. 8 shows the energy cascade process categorizing into three distinct ranges: energy containing range with large scales, inertial range where only the inertial effects are prominent and the dissipation range where viscous effects are most important.

In order to achieve the scale separation, the equations of motion are filtered. LES approximates the real flow to the smallest scales that is resolved by the grid and and scales not captured by the grid(*sub-grid scales*), which are also significant in the flow, are *modeled*.

D. Review of Past Work

1. Experiments

Flow separation is remarked as one of the unsolved problems in fluid mechanics [6]. Early work on laminar separation bubbles by Owen [12] lead to classifications, *short* and *long* separation bubble based on the ratio of bubble length and displacement thickness of the boundary layer. Short bubbles tend to have little parasitic effect on the drag of the blade but long bubbles affect the drag and lift significantly. The ratio l/δ_1 of 100 and 10000 classifies the bubble as short and long. In the present study, a rather short laminar separation bubble is investigated. However, Gaster [13] deduced the dependence of the bubble behavior on the Re and pressure gradient by using the momentum thickness of the boundary layer instead of displacement thickness used in [12] amongst others. The change in momentum thickness is small in the regions of separation as compared to the displacement thickness and so would remain fairly constant in the boundary layer.

In turbines and compressors, the trailing edge thickness of rotors produce wakes that impinge on the stators and vice-versa. Through a set of experiments, Hodson et al. [14] investigated the effects of upstream wakes in a rotor and found that the transition moved upwards on the suction surface as Re is lowered. At low Reynolds Number, the fluid has lesser kinetic energy near the boundary layer and is susceptible to the adverse pressure gradient much upstream. More importantly, wake-induced transition prevented the laminar separation in their study. A similar observation was made by Hilgenfeld et al. [15] who observed a reduction in time mean total pressure loss due to the wake impact. Schobeiri et al. [8] concluded that when the maximum wake fluctuation is less than the time mean fluctuation, the wakes have an impact on the transition. This shows the sensitivity of separation bubble to external

disturbances and fluctuations since the wakes increase the freestream disturbance by locally increasing the turbulent intensity. Experimental investigations have been conclusive in identifying the transition mechanism, effects of wake and free-stream turbulence. However, boundary layer measurements in experiments are plagued by the lack of directional information of velocity. This is because a single-wire probe gives the velocity only in the direction of flow and not its component. Also, it is difficult to observe and quantify the flow structures, the formation and stretching of vortices that are usually found in transitional flow. The ease of availability of these combined with the availability of spatial and temporal information of the flow have been a source of motivation for computational investigations of transition.

2. Simulations

Computational investigations of laminar separation bubbles were started as early as 1970 by Briley [16] using a 2-D finite difference scheme. However recent investigations by Alam and Sandham[5] report that two-dimensional simulations are inaccurate in capturing many of the basic physics of separation. In their study, the two-dimensional simulation under-predicted the bubble length by 40% and skin friction by 50% as compared to a 3D simulation. The transition to turbulence was found to be through the formation of hairpin vortices in the reattachment regime of the flow. Meara et al. [17] investigated the effects of Re and angle of attack on the bubble behavior. As the Reynolds number was increased, the bubble reduced in size while at higher angles of attack the length of separation bubble increased. This could be attributed to the inherent inertial force at high Re that counters the adverse pressure gradient better but not sufficient to avoid separation. At higher angles of attack the adverse pressure gradient is higher and so the bubble develops further. Also they measured the separation angle to calculate the height of recirculating region in the bubble and

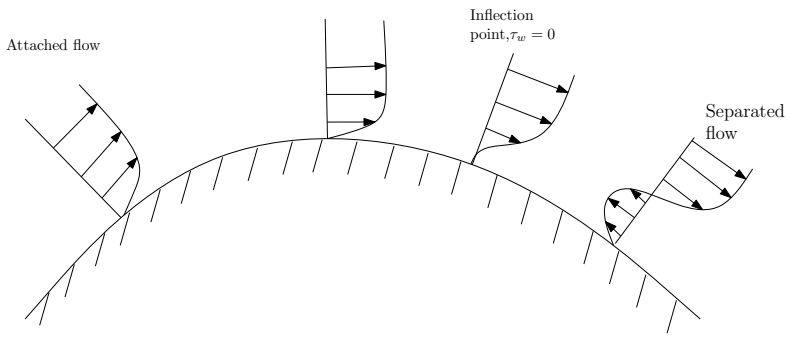

Fig. 9. Velocity profiles prior and aft-separation. At the point of separation, also known as inflection point, the wall shear stress vanishes.

also to benchmark for semi empirical transition models. The separation angle has also been used to find the existence of Görtler instability in Inger [18].

The start of separation is generally taken as the point at which the wall shear stress vanishes. A generic velocity profile prior and aft-separation is shown in Fig. 9. In this, the flow accelerates till the highest point of the hump and begins to decelerate henceforth. Separation sets in further downstream indicted by vanishing shear stress at the wall but the flow does not reattach.

In low pressure turbines, the transition to turbulence is indicated in the pressure curve by a sudden pressure recovery. This is usually accompanied by enhanced mixing and mass transfer between the freestream and the bubble [8]. The onset of separation and transition and the reattachment point is identified in the pressure curve in Fig. 10. The pressure in the laminar region ST is fairly constant and then there is a rapid increase in the pressure showing signs of turbulence. The end of this rapid increase in pressure is associated with the reattachment of boundary layer [17].

Large scale computations including Direct Numerical Simulation have been performed on a LPT cascade. However, the simulation by Kalitzin at al. [19] suffered significantly from grid resolution near the leading and trailing edge of the blade and

Table I. Review of grid resolutions used and type of study conducted. Computational investigations by Kalitzin et al. [19] and Wissink et al. [20] suffered from lack of resolution while the study by Michelassi et al. [21] focused on effect of wakes on transition. The present study investigates the mechanism causing the transition using a highly resolved LES. The non-dimensional wall distances are calculated based on the shear stress at $s/s_o = 0.73$ and values at the first grid point are reported here.

Authors	Method	Δx^+	Δy^+	Δz^+	Type
Present Study	LES	$\sim$2	$\sim$0.25	$\sim$2	Turbine
Alam and Sandham [5]	DNS	14-20	0.5	$\sim$1.0	Flat plate
Yang and Voke [22]	LES	10-30	1	9	Flat plate
McAuliffe et al. [23]	LES	19	0.5	19	Flat plate
Roberts and Yaras [24]	LES	36	0.8	38	Flat plate
Kalitzin et al. [19]	DNS	28	2.3	1.9	Turbine
Wissink et al. [20]	LES	40-60	2$\sim$4	10-20	Turbine
Michelassi et al. [21]	LES	65	$<$5.5	15$\sim$20	Turbine

skewness in the passage showing signs that an accurate and highly resolved DNS with the current resources is far-fetched. LES seems to be a more viable option in terms of grid resolution since only the energy carrying large scales are resolved which requires a fairly coarse mesh. Pauley et al. [25] conducted LES with a dynamic Smagorinsky model and a sensitivity analysis with several filter parameters. They observed overshoot and undershoot in the pressure distribution at the start and end of transition due to vortex shedding. It has been reported that the shedding is aperiodic with single frequency and a range of values are reported in Yang and Voke [22]. This unsteadiness of the separated shear layer is known as low frequency flapping and the

flapping frequencies range from $0.12-0.2U_\infty/l$. The study did not yield any optimum value of the filter width. The no sub-grid model LES did not result in any agreeable values of pressure distribution and their study suggest an inclusion of sub-grid scale models. Interestingly, they found the results of a 2-D LES comparable to experiments as compared to many 3-D LES computations.

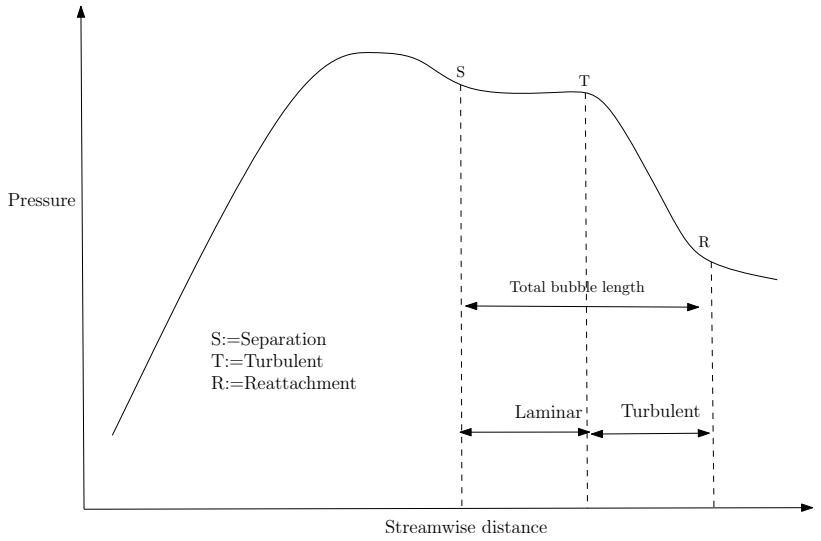

Fig. 10. Schematic of separation and reattachment in laminar separation bubbles as given in Horton [26]. The constant pressure region inside the bubble is usually the laminar regime while the turbulent regime is characterized by the rapid decrease in pressure, the end of which signifies the reattachment of boundary layer.

Yang and Voke [22] implemented a LES on reattaching boundary layers in a flat plate using dynamic smagorinsky model. They observed the instantaneous separation bubble length to be more than 50% of the time mean bubble length and attributed it to the violent and highly unsteady nature of the flow near the reattachment regime. This shows that the time averaged bubble length could under-predict the drag and several other parameters and motivates a need for unsteady analysis of the dynamics

of flow downstream of reattachment that are difficult to carry out experimentally. The development of Kelvin-Helmholtz instability in the separated shear layer is believed to have caused the transition which is also in agreement with investigations of Brian et al. [23].

The table I summarizes, from literature, the type of geometry used in the simulations and the resolution in non-dimensional wall units. For the present study, the wall shear stress is measured at 73% ($s/s_o = 0.73$) of suction side and minimum values are reported in the table. As can be seen, many simulations have been done with flat plate and inducing a pressure gradient by contouring the wall, suction or by other means to replicate the conditions that would trigger transition. This however fails to replicate the exact flow physics like the distortion of wakes at the leading edge that is present in a cascade [27]. The present study precisely depicts the cascade environment in a low pressure turbine. Using a dynamic eddy viscosity model, Michelassi et al. [21] attempted to characterize the flow structures on the suction and pressure surface with the presence of wakes. Their study yielded agreeable results for pressure surface but the fine scale structures on the suction side were not captured because of under-resolved regions.

The behavior of the bubble and transition is very sensitive to the choice of subgrid models used in LES. There has been several studies in developing a suitable SGS model that would accurately predict transitional flows. Such a model should predict vanishing values of eddy viscosity when the flow is laminar and must also provide adequate dissipation when the resolution is coarse. In computations, the eddy viscosity is usually clipped to positive values for stability reasons eliminating the prediction of back scatter that is found in some turbulent flows [28]. Recently, Schlatter et al. [29] applied Approximate Deconvolution Model (ADM) to transitional flows where the unfiltered values for non-linear terms are replaced by a inverse filter operation. With

a rather coarse grid, the results of LES were in close agreement with DNS. The inverse filtering operation can be seen as a High Pass Filter(HPF) in frequency domain. The present study investigates the effectiveness of a HPF Smagorinsky model in prediction of transition.

3. Transition Mechanism and Instabilities

The transition mechanism starts with a Kelvin-Helmholtz instability of the shear layer which results in formation of spanwise roll-up vortices. The subsequent breakdown of these spanwise vortices into smaller structures is believed to cause the transition to turbulence and thus the reattachment [23]. The laminar flow is extremely sensitive to external disturbances and any small fluctuation in the freestream causes a instability, the amplification of which triggers the transition. The fluctuations can be due to free stream turbulence, vortices shed from the previous stage, pressure fluctuations, noise or any other form of disturbance. In order to simulate these conditions, disturbance in terms of freestream turbulence is generated in the present study. When the disturbances grow in space, the type of instability associated is convective, and absolute instability if the growth is in time [5]. In convectively unstable flow, the disturbances convect and grow away from the source, while in absolutely unstable flow, the disturbance spread everywhere in space and time [22].

Most of the studies on separation and reattachment has been done with a flat plate which fails to replicate the conditions in a cascade. In this study, a highly resolved low pressure turbine cascade is used to study the mechanism of transition and in identifying the dominant flow structures on the suction and pressure surface. The present study also attempts to validate a HPF eddy viscosity model that accounts for the interaction between the unresolved small scales and the resolved scales. The application of a HPF eddy visocisty models to transitional flows in turbomachinery

has not been investigated yet.

CHAPTER II

HIGH PASS FILTERED EDDY VISCOSITY MODEL

The scale separation into large and small scales is done by filtering the Navier-Stokes equation using a low pass filter [28]. The filter essentially smoothens the computed solution to resemble the exact solution as shown in Fig.11. The resolved and modeled scales in LES is figuratively shown in Fig. 12. This chapter is organized as follows. Definition of filter and its types are discussed, followed by sub-grid viscosity model. A comparison of RANS approach to LES is also discussed. A high pass filtered eddy viscosity model is introduced and an attempt is made to validate it for a flow over a flat plate with hemispherical protuberance.

A. Filter

Leonard [30] proposed the filtered component to be,

$$\bar{\phi}(x,t) = \int_{-\infty}^{\infty} \phi(\xi,t) G(x-\xi) d\xi, \tag{2.1}$$

where $G(x-\xi)$ is the convolution kernel of the filter. Some of the commonly used filters are Gaussian and Tophat that are shown in Fig. 13 with their corresponding transfer functions given in Eqn.2.2 and Eqn. 2.3:

$$\hat{G}(k) = \exp\left(\frac{-\overline{\Delta}^2 k^2}{4\gamma}\right), \gamma = 6. \tag{2.2}$$

$$\hat{G}(k) = \frac{\sin(k\overline{\Delta}/2)}{k\overline{\Delta}/2}. \tag{2.3}$$

Applying the filter from Eqn. 2.1 on Navier-Stokes equation, the filtered NSE becomes,

$$\frac{\partial \bar{u}_i}{\partial t} + \frac{\partial}{\partial x_j}\left(\overline{u_i u_j}\right) = -\frac{1}{\rho}\frac{\partial \bar{p}}{\partial x_i} + \nu \frac{\partial}{\partial x_j}\left(\frac{\partial \bar{u}_i}{\partial x_j} + \frac{\partial \bar{u}_j}{\partial x_i}\right), \tag{2.4a}$$

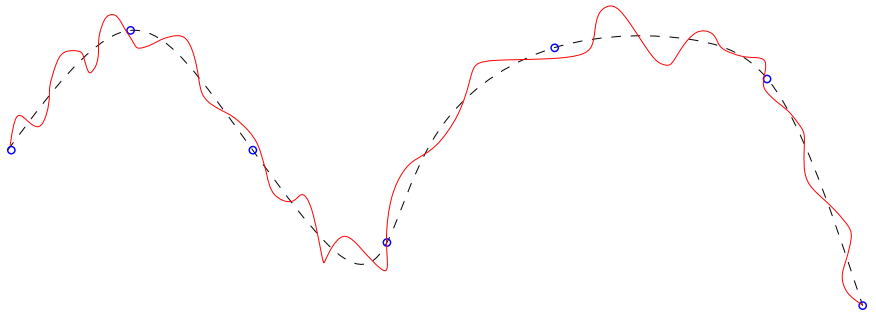

Fig. 11. The exact solution is represented by the red curve while a filtered velocity field will resemble the dashed lines. The filtering operation can be seen as smoothing the high frequency computed velocity.

$$\frac{\partial \bar{u}_i}{\partial x_i} = 0, \tag{2.4b}$$

where quantities with an overbar indicate filtered quantities. As can be seen the non-linear terms in the Eqn. 2.4a cannot be computed directly, since only $\bar{u}, \bar{p}$ are known. In order to avoid that,the following decomposition is used,

$$\frac{\partial \bar{u}_i}{\partial t} + \frac{\partial}{\partial x_j}\left(\bar{u}_i \bar{u}_j\right) = -\frac{1}{\rho}\frac{\partial \bar{p}}{\partial x_i} + \nu \frac{\partial}{\partial x_j}\left(\frac{\partial \bar{u}_i}{\partial x_j} + \frac{\partial \bar{u}_j}{\partial x_i}\right) - \frac{\partial \tau_{ij}}{\partial x_i}, \tag{2.5a}$$

$$\tau_{ij} = \overline{u_i u_j} - \bar{u}_i \bar{u}_j. \tag{2.5b}$$

where τ_{ij} is modeled. It is also to be noted that, the non-linear term $\bar{u}_i \bar{u}_j$ contains information from frequencies higher than the individual frequencies of $\bar{u_i}$ and $\bar{u_j}$. To include all such information, a much higher degrees of freedom is required which is usually achieved by de-aliasing the non-linear terms [28].

A popular way of modeling the sub-grid scales is using an eddy viscosity model. The premise here is that the small scales are universal and its role in the energy cascade is to dissipate the energy which could be accomplished by adding an artificial viscosity(known as *eddy viscosity*) to the flow. Unlike molecular viscosity, the eddy

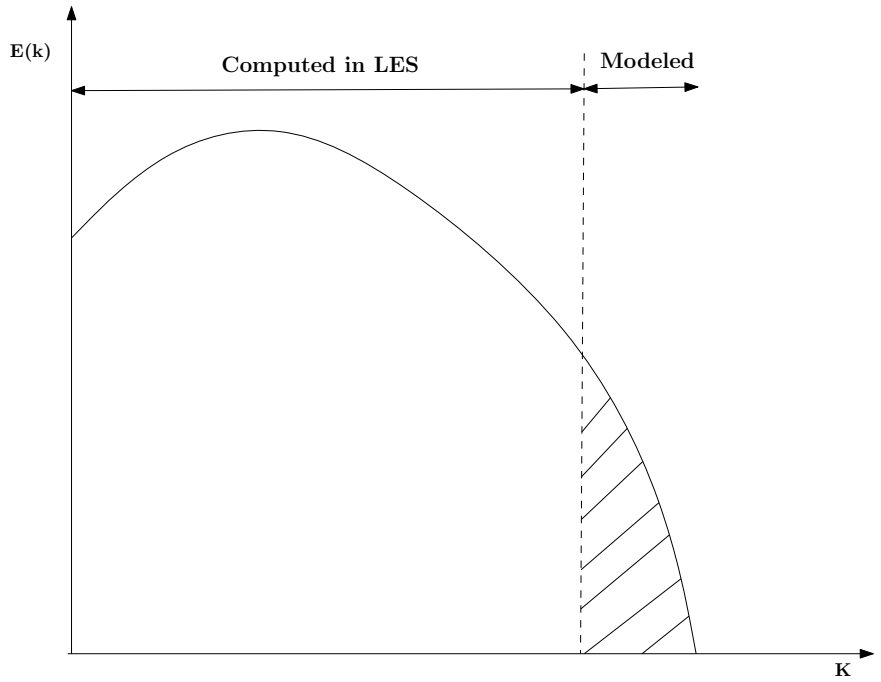

Fig. 12. Representative figure of energy spectrum in a LES as shown in [28]. The effect of smaller scales that are significant in the flow are modeled.

viscosity is not dependent on the fluid but rather on the flow itself and so changes according to the behavior of flow. These models that employ artificial viscosity for sub-grid scales are known as sub-grid viscosity models.

1. Sub-grid Viscosity Models

As mentioned above, the sub-grid viscosity based models relate the deviatoric part of stress tensor, to the strain rate by eddy viscosity,

$$\tau_{ij} - \frac{1}{3}\delta_{ij}\tau_{kk} = -2\nu_t \overline{S}_{ij}, \tag{2.6a}$$

$$\overline{S}_{ij} = \frac{1}{2}\left(\frac{\partial \bar{u}_i}{\partial x_j} + \frac{\partial \bar{u}_j}{\partial x_i}\right), \tag{2.6b}$$

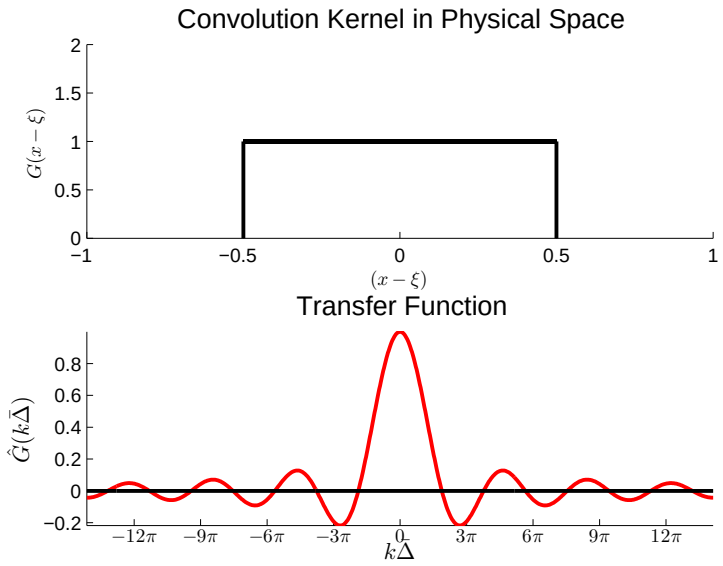

(a)

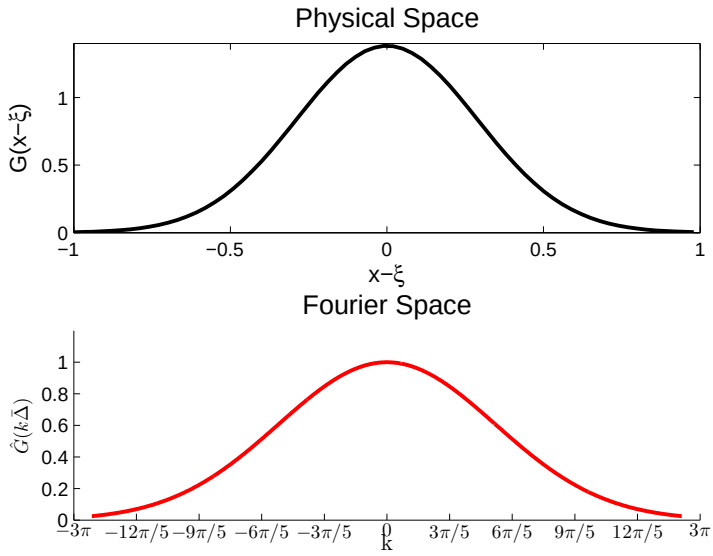

(b)

Fig. 13. Convolution kernel and transfer function of (a) Tophat and (b) Gaussian filters as discussed in Sagaut [28].

where ν_t is the eddy viscosity that depends on the flow characteristics and $\overline{S}_{ij}$ is the mean rate of strain. In Smagorinsky model ν_t is defined by,

$$\nu_t = (C_s\overline{\Delta})^2(2|\overline{S}(x,t)|^2)^{\frac{1}{2}}, \tag{2.7a}$$

$$\overline{\Delta} = (\Delta x \Delta y \Delta z)^{\frac{1}{3}}\,, \tag{2.7b}$$

where $\overline{\Delta}$ is the filter width that is usually defined by Eqn. 2.7b, the constant C_s is calibrated depending on application. However the dynamic version of the model, allows a spatially varying constant that could also take negative values indicative of the backward energy cascade [28]. Since, a negative value of C_s would destabilize the flow, it is usually clipped to positive values.

2. High Pass Filtered Smagorinsky Model

The low pass filter typically allows the information from low frequency components and masks the high frequency information. Therefore the interaction between the high frequency components (small scales) and low frequency components (large scales) is lost in the model. But in high pass filtered Smagorinsky model, the interaction between the unresolved small scales and the largest resolved scales are accounted by using an high pass filtered strain rate for modeling the eddy viscosity [29].

$$\nu_t = \left(C_s^{HPF}\Delta\right)^2 |S(H*u)|, \tag{2.8a}$$

$$|S(H*u)| = \sqrt{2S_{ij}(H*u)S_{ij}(H*u)}, \tag{2.8b}$$

$$\Delta = \sqrt[3]{\Delta x_1 \Delta x_2 \Delta x_3}, \tag{2.8c}$$

$$C_s^{HPF} = \frac{\pi}{\pi - \omega_c} C_0, \tag{2.8d}$$

where $C_0 = 0.1/3$ when $\omega_c \simeq 2\pi/3$ and $S(H*u)$ is the high pass filtered strain rate.

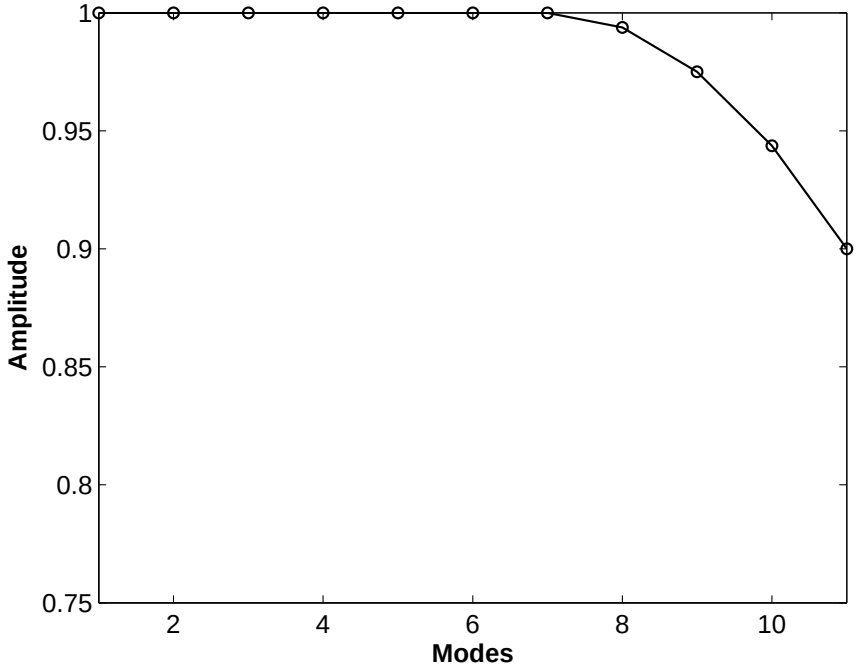

Fig. 14. Transfer function of the stabilizing filter for the spectral element basis function. Here the last 4 modes are filtered by a quadratic function with a weight of 0.10.

3. Stabilizing Filter

A stabilizing filter that dampens the high frequency components(velocity and pressure) developed by Fischer [31] is used in the present study. The filter is applied after each step and preserves inter-element continuity [31]. In the present study, the filter shown in Fig. 14 is applied for the last 4 modes with a weight of 0.10.

B. Comparison to RANS

A comparison can be drawn to RANS which is based on the premise that the instantaneous velocity is a sum of steady and fluctuating term,$\mathbf{U}(\mathbf{x},t) = \bar{\mathbf{U}}(\mathbf{x}) + \mathbf{U}'(\mathbf{x},t)$. The deficiency in RANS for predicting transitional flows could be attributed to atleast

two factors,

1. The mean velocity is assumed to be the time-averaged while separation/transition is an instantaneous phenomenon.

2. The flow is anisotropic but RANS force isotropy in normal stresses and assume the Reynolds stress is proportional to the mean rate of strain at every spatial location and time instant. The anisotropic part of Reynolds stress, $\overline{u_i u_j} - \frac{2}{3} k \delta_{ij}$ is forced to follow the dynamics of mean strain rate by an eddy viscosity [10]. The idea of relating the stress with the strain rate($\bar{S}_{ij}$) is in conjunction with Newton's law($\tau_{ij} = 2\mu S_{ij}$) but associating non-linear term $\overline{u_i' u_j'}$ as stress is questionable.

But in LES, the large scales of motion are calculated explicitly and the small scales that are universal and isotropic are modeled resulting in a better treatment of the stress term. The computational affordability and the accuracy of solution in predicting the flow physics are some of the factors for the gaining popularity of LES. A schematic comparison of RANS and LES is shown in Fig.15 that shows the resolved and modeled scales of motion for both.

C. Numerical Set-up

In order to validate the HPF Smagorinsky model, flow over a flat plate with hemispherical protuberance is chosen. A Reynolds number of 3500 based on freestream velocity and diameter of hemisphere is chosen for the DNS and LES simulations. A nearly isotropic turbulence is generated by a recycling method introduced by Stolz and Adams [32] and developed at FT^{2}L. At a certain distance downstream of the inflow plane a recycling plane is chosen from which the mean velocity values are scaled such that the volume averaged velocity inside the box is one and copied to the inflow

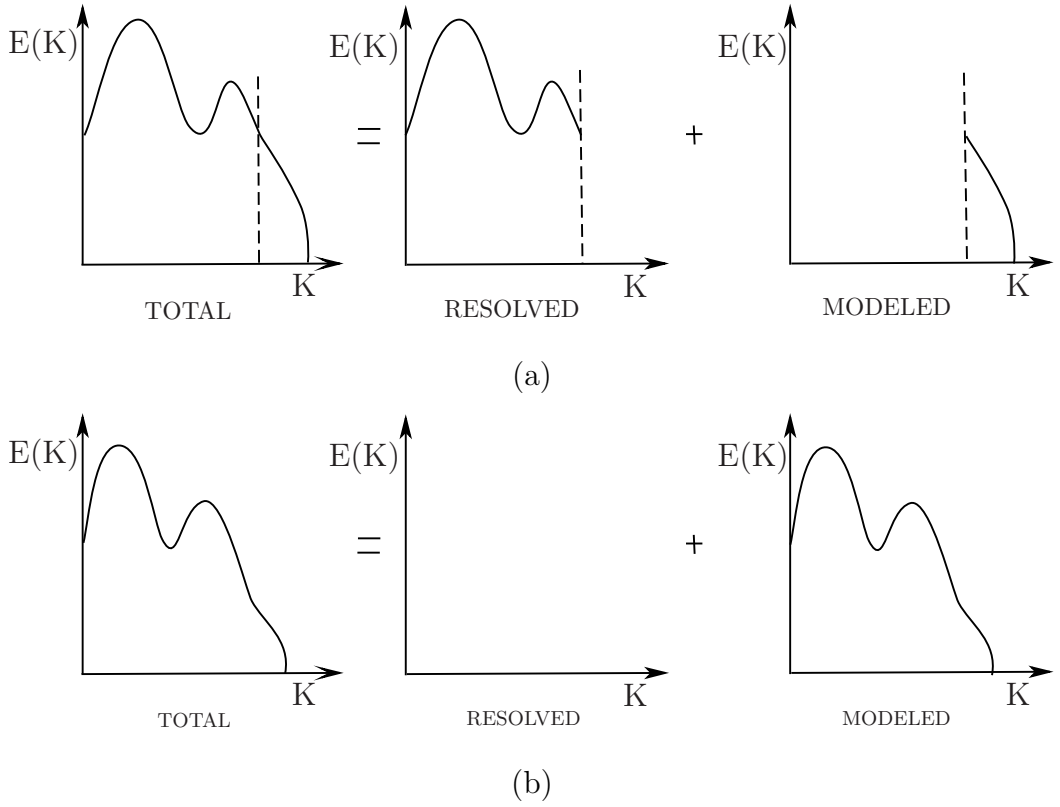

Fig. 15. Decomposition of energy spectrum in LES and RANS as illustrated by Sagaut [28]. The characteristic large scales are resolved in LES, and the significant contributions form small scales are modeled but in RANS, the entire flow field is modeled.

boundary. Without scaling, the energy inside the box would dissipate continuously and turbulence will eventually decay. Also, a fully developed turbulence can be generated within a short streamwise distance by rescaling and recycling [32]. The inflow plane at $Z/D = -5.0$ and the recycling domain is initialized with multiple vortices, the stream function of which is given by Eqn. 2.9b

$$-\nabla^2\psi = \lambda\psi, \tag{2.9a}$$

$$\psi = \frac{1}{4}\cos(3z)\sin(4y) - \frac{1}{5}\cos(5y) - \frac{1}{5}\sin(5z). \tag{2.9b}$$

At $Z/D = 0.0$, a flat plate initiates the formation of boundary layer upstream of

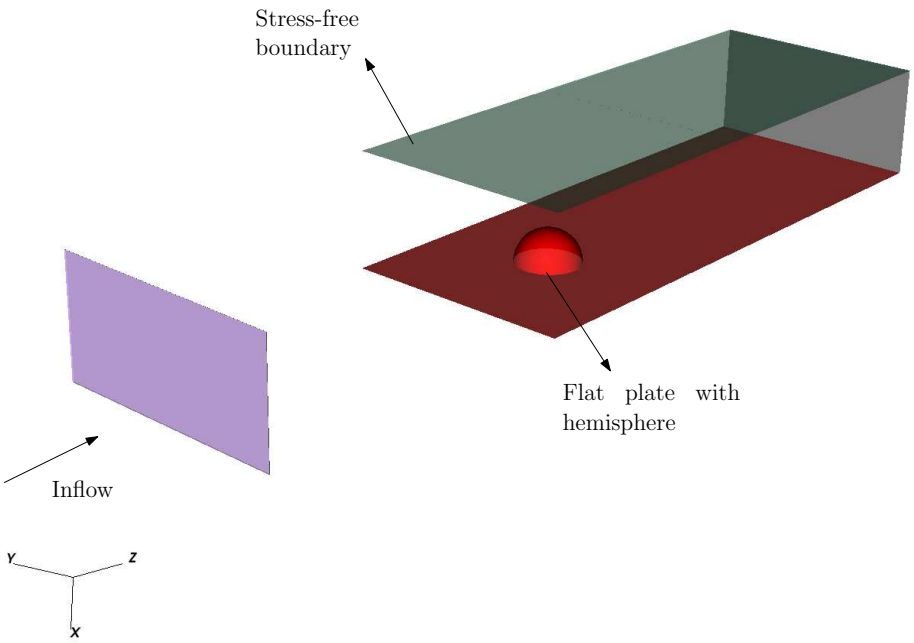

Fig. 16. Flow domain shown without periodic faces. A recycling plane is chosen downstream of the infloe plane from which the mean velocity values are scaled such that the volume averaged velocity inside the box is one and copied to the inflow boundary. A stress free boundary condition is used for the pitchwise direction after the periodic box.

the hemisphere that is stationed at $Z/D = 2.0$. The domain between the wall and the inflow plane is periodic in the spanwise and pitchwise direction to preserve the homogeneity in the flow. The flow domain without periodic faces is shown in Fig. 16. Inside the recycling domain, at $Z/D = 0.25$, a recycling plane is chosen, the velocities of which are scaled and copied to the inflow plane. In the pitchwise direction, a stress free boundary condition is used. The outflow plane is positioned at $Z/D = 9.0$. The drag on the hemisphere and velocity profiles downstream of the hemisphere are

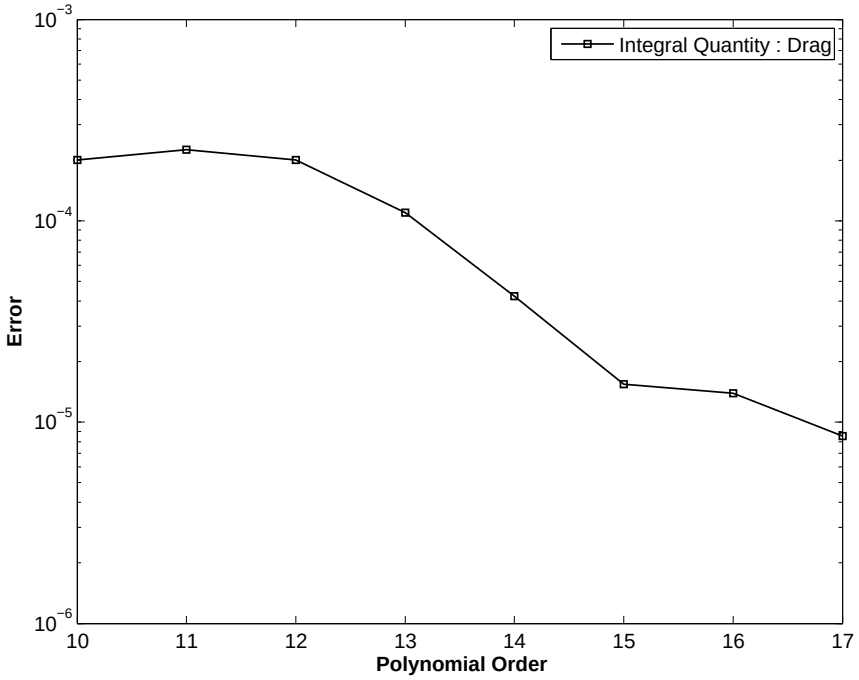

Fig. 17. Exponential convergence showing grid independence. The DNS is carried out at a polynomial order of 14.

monitored for comparing LES against the DNS. It is to be noted that periodic hairpin vortex structures were observed in the laminar wake behind the hemisphere under the conditions of a laminar flow by Acarlar and Smith [33].

A total of 60 Million grid points is used for the DNS with an interpolation polynomial order of 14 for each element. A p-type refinement was performed for convergence study which showed exponential convergence as shown in Fig. 17.

D. Results and Discussion

Time mean velocity profiles at different streamwise locations are presented in the Fig. 19 that compares the DNS and the HPF Smagorkinsky model. The HPF Smagorinsky model is implemented on a grid that is approximately 6 times coarser

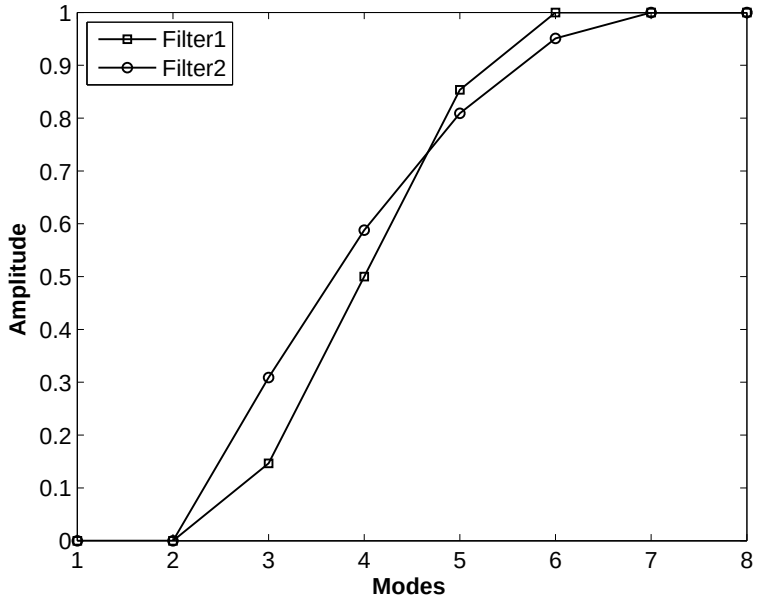

Fig. 18. Transfer function of different High Pass Filters considered. The filter is set similar to a cosine function starting from mode 6 and 7 respectively. The filters are denoted as filter1 and filter2.

than the grid used for DNS. This would activate the filter in under-resolved regions. Both the simulations span over the same time interval so that the dynamics of the flow could be compared.

1. Time Mean Velocity Profiles

The transfer function of different filters used are plotted in Fig. 18. Time mean velocity profiles at 0.5D,1.5D and 2.5D downstream of the hemisphere are plotted for the DNS and HPF Smagorinsky model in Fig. 19.

a. Filter1

The filtered velocity profile is in fair agreement with the DNS at 1.5D downstream of the hemisphere, where D is the diameter of the hemisphere. At 1.5D, minor reverse flow is observed in both the DNS and LES simulations. The LES predicts well until $y/D = 0.30$, after which the predictions are off as compared to the DNS. At 2.5D, LES predicts an opposite trend as compared to the DNS.

b. Filter2

The filter over-predicts the flow reversal at 1.5D, but follows the general trend predicted by the DNS. For velocity profile at 2.5D, the filter is in very good agreement with the DNS. Since this filter did not yield a reasonable comparison to the DNS at 1.5D, other filter functions need to be tested for modeling the SGS terms.

The results of filter1 is in close comparison to the DNS at 0.5D and 1.5D downstream of the flow and hence is chosen for the production runs. The streamwise rms velocity comparison for filter1 and DNS is shown in Fig. 20. The general trend is predicted well at 0.5D and 1.5D downstream of the hemisphere.

2. Coherent Structures

Coherent structures were observed downstream of the hemisphere in both the DNS and LES simulations. The hairpin vortices shown in Fig. 21 were observed using the λ_2 method developed by Jeong and Hussain [34]. These vortices begin to evolve in the wake of the hemisphere and extend into the freestream. But due to the high freestream turbulence and flow acceleration, the structures don't persist more than four-five diameters downstream of the hemisphere.

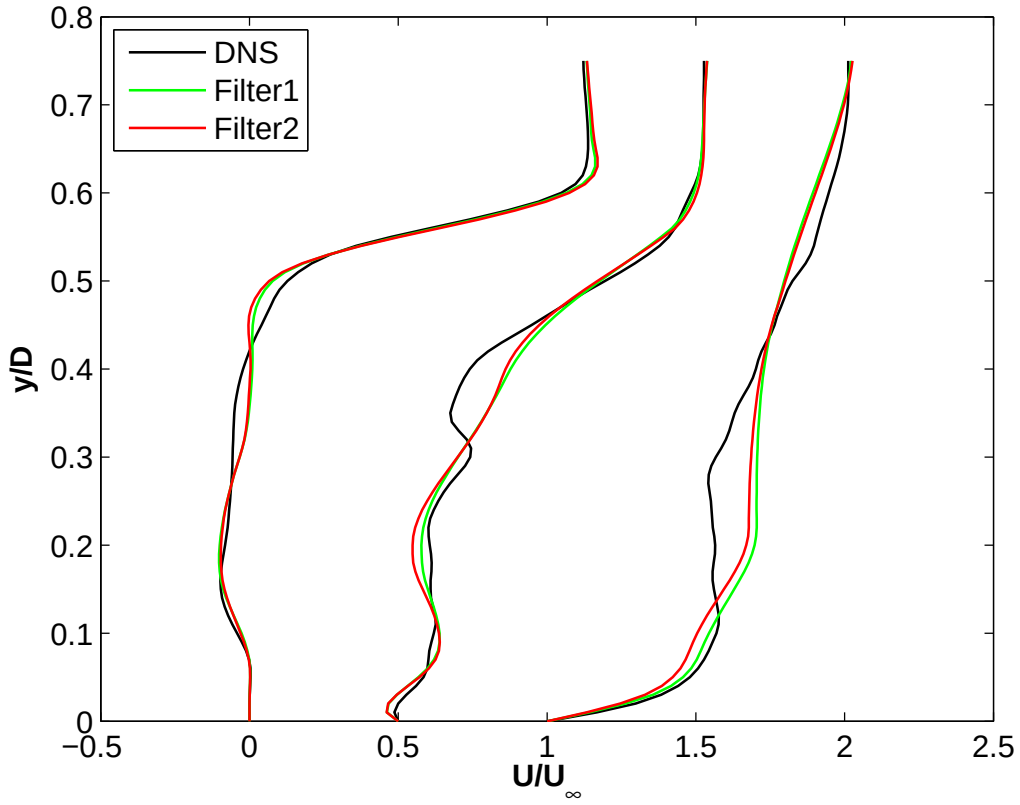

Fig. 19. Time mean mid section velocity profiles at 0.5D, 1.5D and 2.5D downstream of the hemisphere. The velocity profiles are offset by 0.50 in X-axis for clarity. The profiles are in fair agreement with the DNS at 1.5D, but fails to follow the trend of DNS at 2.5D downstream.

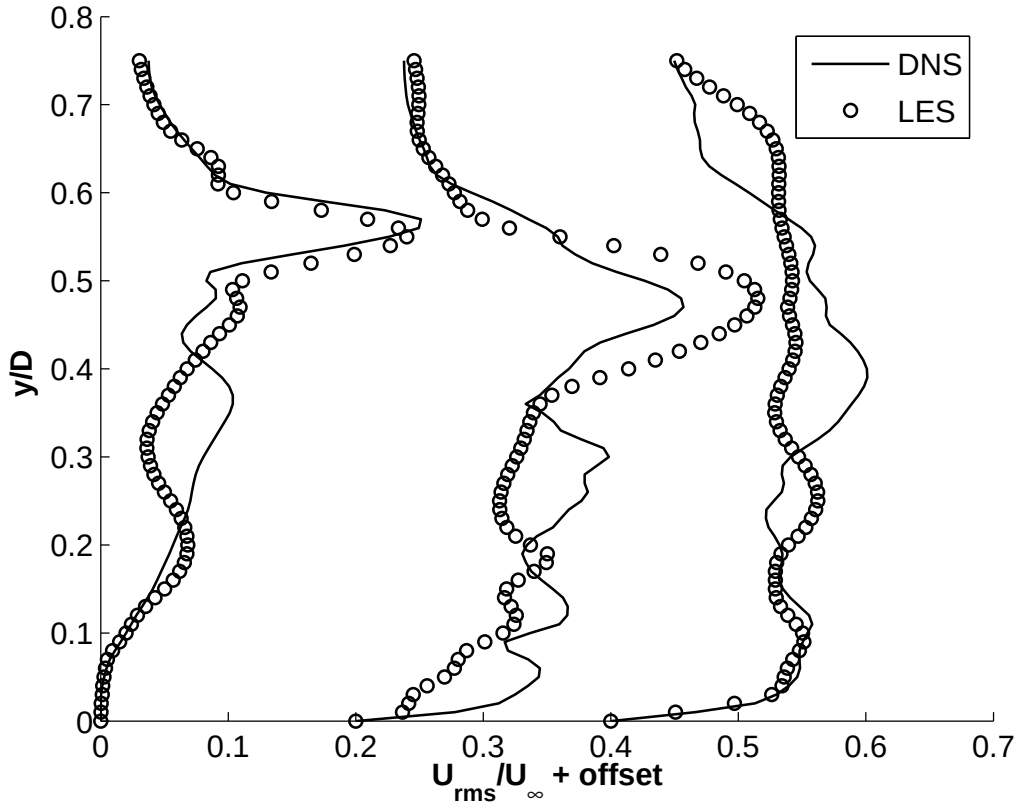

Fig. 20. Streamwise rms velocity profile at 0.5D, 1.5D, 2.5D donwstream of the hemisphere. The general trend of DNS profiel is predicted well at 0.5D and 1.5D downstream of the hemisphere.

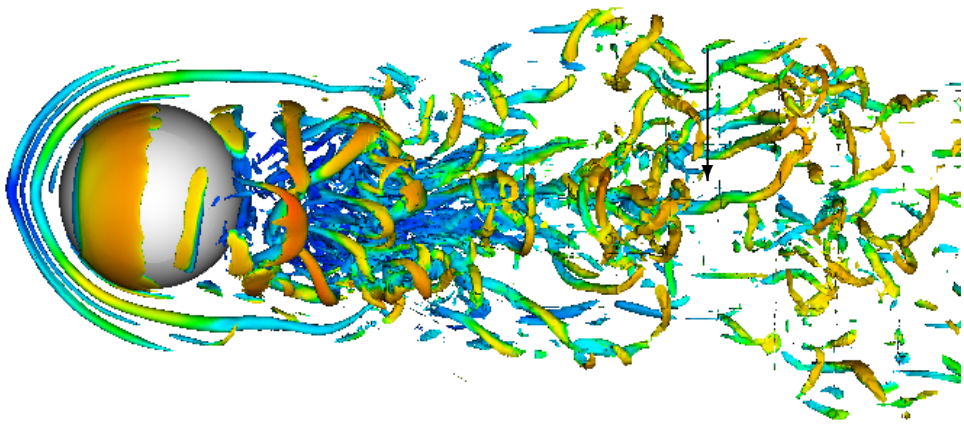

Fig. 21. The hairpin vortex can be seen in the wake of hemisphere. The leg of vortex is in velocity deficit region while its head is in the freestream. The arrow points to the leg of a distinct hairpin structure downstream of the hemisphere.

CHAPTER III

APPLICATION TO LOW PRESSURE TURBINE

The applicability of High Pass Filtered Smagorinsky model is examined for flow over a low pressure turbine cascade that exhibits transitional flow on the suction surface. Experimental investigations were conducted by Schobeiri et al. [8] at Re=110,000 based on exit velocity and suction surface length which corresponds to Re=68,000 based on inlet velocity and suction surface length. The chapter is organized as follows: Computational methodologies and description of numerical method are discussed first, results are shown for simulations with a stabilizing filter for spectral element basis function and with the HPF Smagorinsky model for the sub-grid scales.

A. Description of Flow Domain

The flow domain has been chosen to match the experimental set up of Schobeiri et al. [8]. The parameters matched are the Re, turbulence intensity, cascade solidity and the inlet flow angle. The Re based on suction surface length and inlet velocity is set by having a unity free stream velocity and changing the viscosity accordingly. A single blade in the cascade is considered with periodic boundary conditions in the pitch and spanwise direction. The computational domain in entirety is shown in Fig. 22(a). A nearly isotropic turbulence is generated by allowing a divergence free velocity field with multiple vortices at the inflow plane($y - z$), $X/C_{ax} = -5$, to advect inside a doubly-periodic box. The periodic box does not introduce any shear layer and thus preserves the vortical structures in the flow. The energy is then redistributed by an array of bars, at $X/C_{ax} = -4.5$, and turbulence is allowed to decay. The divergence free velocity field for a periodic box, also known as Eddy solutions of Navier Stokes Equation, is given by Eqn. 2.9a and 2.9b where λ is the eigenvalue and is related

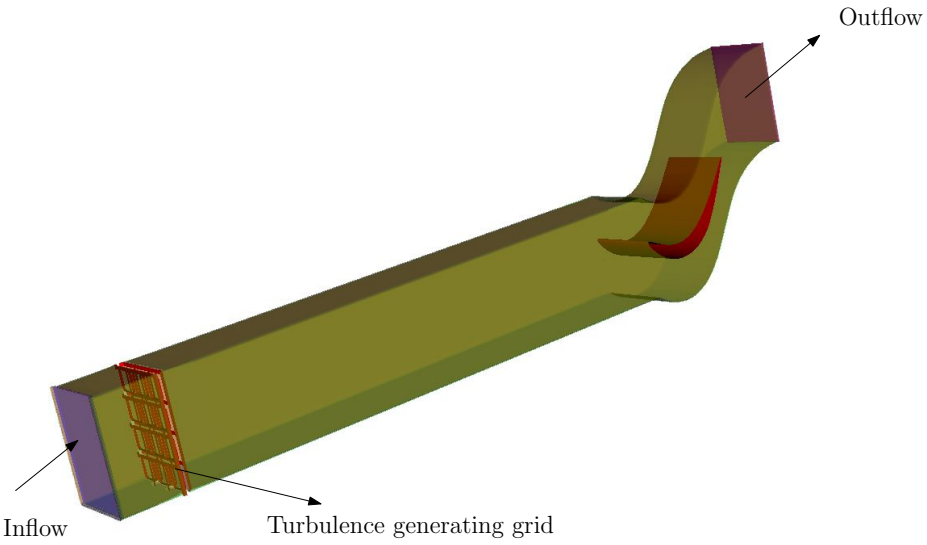

(a)

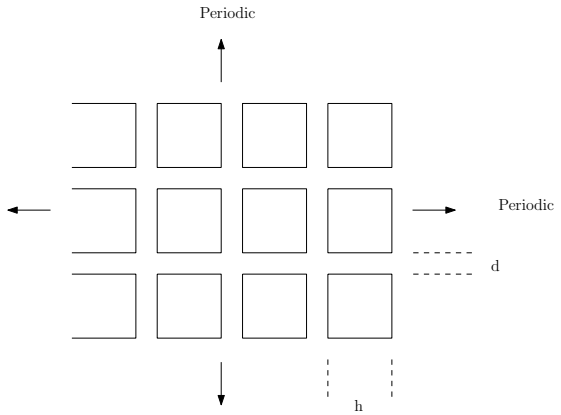

(b)

Fig. 22. (a): Descriptive figure of the flow domain showing the inflow and outflow boundaries with the array of turbulence generating bars.(b): Grid used for generating isotropic turbulence. The aspect ratio of the grid can also be changed to vary the length scales of flow.

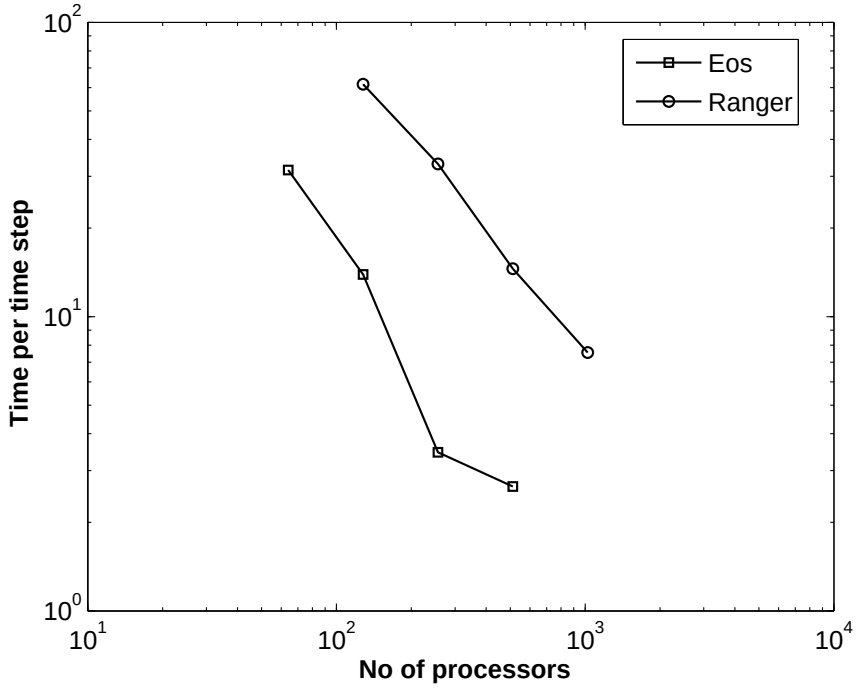

Fig. 23. Strong scaling of NEK5000 for two different computer architectures: EOS at Texas A&M Supercomputing Center and Ranger at Texas Advanced Computing Center(TACC).

to the wavenumber of sines and cosines by, $\lambda = (m^2 + n^2)$, where m and n belong to Natural numbers and ψ is the stream function. One possible combination that is used in the present study is given in Eqn. 2.9b. The values of m, n govern the number of vortices at the inlet plane and could be varied to vary the turbulence intensity and length scales downstream. The contour plot of vorticity is also shown in Fig. 24(b). Since the vortices are super-imposed on the mean flow, the Re of the flow is not changed by changing the wavenumbers. The flow is simulated under conditions of incompressibility since compressible effects come into effect only towards the trailing edge of the blade. An equal order interpolant for velocity and pressure is used for the velocity and pressure since it gives a more accurate treatment of the pressure terms.

Preliminary simulations indicated an angle deviation of about 2° at the inlet of cascade, therefore the angle is offset by 2° at the inflow. The deviation could be attributed to the deflection of the flow just before the cascade. However, minor angle deviations at the inlet were observed experimentally but since no published data is available for the deviation, the angle is made to match the cascade inlet angle by offsetting the inflow. The cascade inlet is matched to the experiment and is at $X/C_{ax} = -0.16$. The length scale at the inlet of the cascade is measured by plotting the auto-correlation coefficient($R(\tau)$) of streamwise velocity. The time scale is defined as the point at which $R(\tau)$ touches zero. The corresponding length scale obtained by multiplying the mean velocity at the inlet is 43.7mm. The plot of auto-correlation coefficient is shown in Fig. 25.

The distance between the stagnation point and the grid can be changed at run-time to achieve a particular value of turbulence intensity. The root-mean-square(rms) of individual velocity components show a similar trend in magnitudes and decay rate as shown in Fig. 24(a) that are characteristics of isotropic turbulence. Since the grid is coarse without an LES model, high frequency modes might appear in the solution that might destroy the otherwise accurate solution. In order to avoid that, a stabilizing filter is applied to the basis function after each time step and filters the last 4 modes by a quadratic function. This would avoid the nonphysical spectral build-up in the energy cascade that is usually found in under-resolved DNS or LES.

B. Numerical Method and Computational Details

A geometrically flexible spectral element solver, NEK5000, is employed that solves the NSE by decomposing the domain into K non-overlapping elements and approximating the solution in each element as series of high order polynomials. Along with the or-

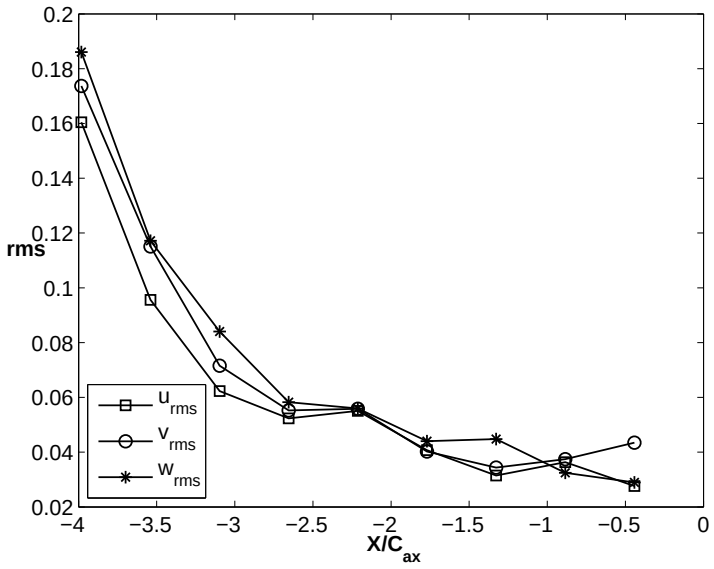

(a)

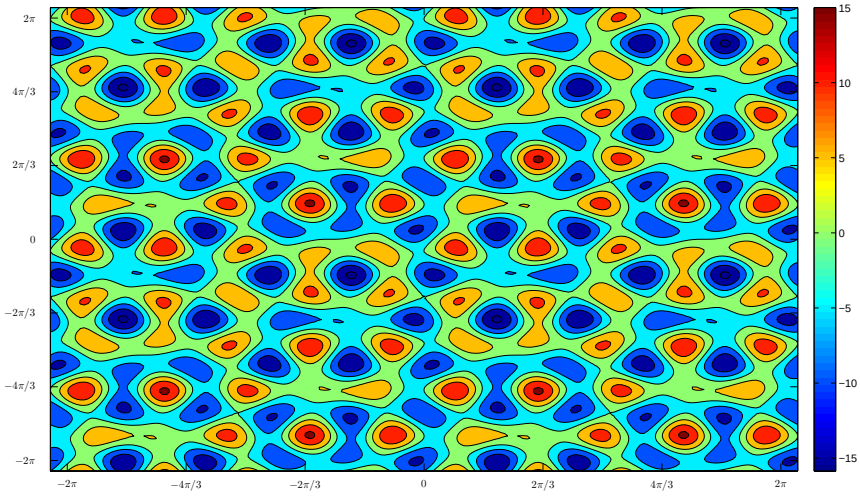

(b)

Fig. 24. (a) Decay of fluctuating components from turbulence generating grid to cascade. A nearly isotropic turbulence is achieved near the leading edge of the cascade.(b) Contour plot of vorticity at a plane on the doubly periodic box. They are scaled to match the inlet and prescribed as inflow boundary condition.

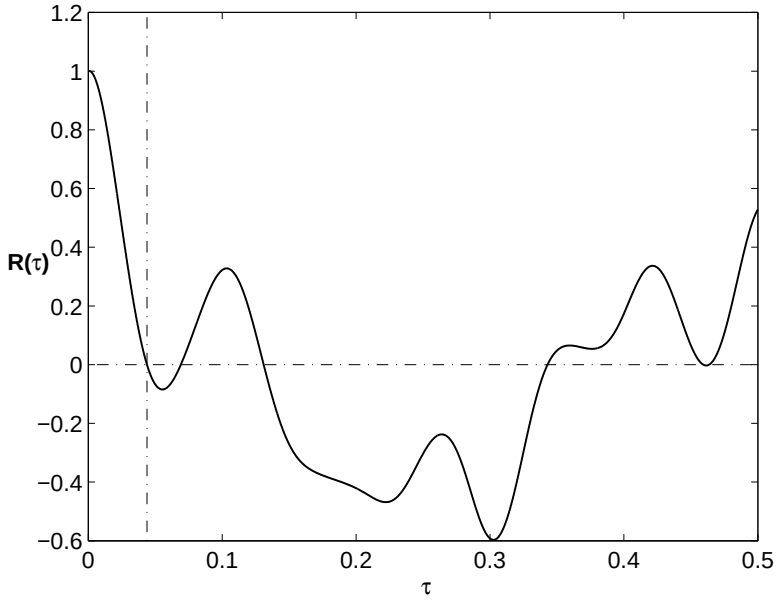

Fig. 25. Plot of auto-correlation coefficient of streamwise velocity component. The time scale is obtained as the time at which $R(\tau) = 0$. The product of velocity magnitude and time scale gives the length scale at the inlet. The length scale noted here is 43.7mm.

thogonal polynomial basis functions and Gauss-Lobatto-Legendre (GLL) quadrature in the reference domain, a high parallel efficiency is achieved [35]. The attractive feature of Spectral element method is the affordability of exponential convergence [31]. A slice of flow domain and exponential convergence achieved in the present study is shown in Fig. 26. Some of the cascade parameters used are shown in Table. II.

Statistical quantities are monitored after reaching quasi steady state. One flow-through time is defined as the average time required for a fluid particle to move from inflow to outflow plane. About four flow-through times are allowed for initial transients to leave the domain and data is subsequently monitored for $1/3^{rd}$ of a flow through. In terms of non-dimensional time units this correspond to $2.25T$, where

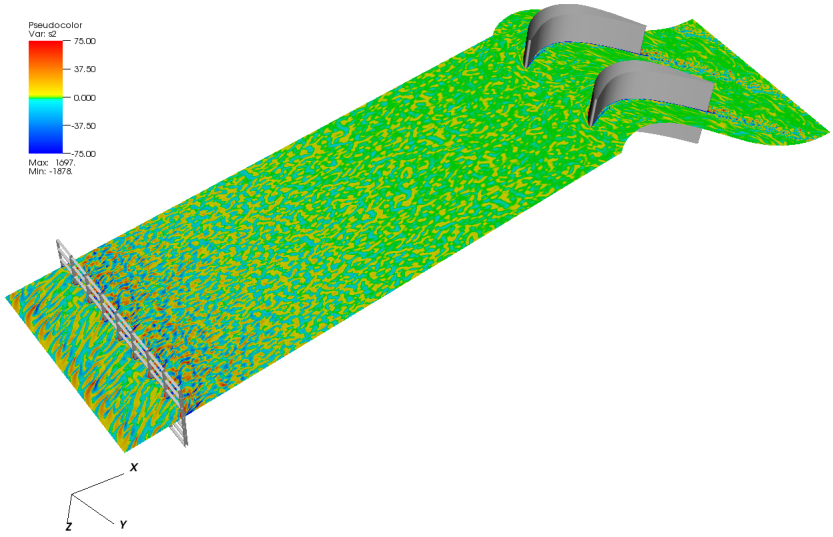

(a)

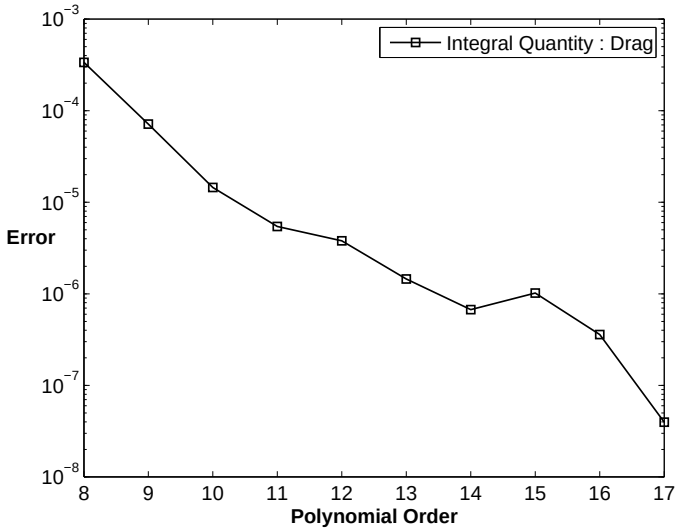

(b)

Fig. 26. (a) Contour plot of spanwise vorticity showing the turbulence generating bars and the blades. Only one-half of the flow domain shown is simulated. (b): A nearly constant slope in semi-log plot of error vs polynomial order signifies an exponential convergence. A polynomial order of 10 is used for the present study.

Table II. The blade cascade parameters normalized with axial chord and freestream conditions used in the simulation are given here.

Parameters	Values	Parameters	Values
Solidity	1.248	Cascade Angle	55°
Re	68000	Chord Length(C)	$1.1C_{ax}$
Re_θ	107	FSTI	3.23%
Bar Upstream Distance	$4.5C_{ax}$	Bar aspect ratio	0.60
Suction Surface Length	$1.45C_{ax}$	Blade height	$0.3985C_{ax}$

T is defined as C_{ax}/U_{ax}. To analyze the time averaged separation bubble, velocity profiles at different locations on the suction side are considered. The velocity profiles are phase averaged at all the points along the spanwise direction but for frequency spectra the time history is obtained by averaging at six equi-spaced intervals along the span.

A highly resolved boundary layer mesh, shown in Fig. 27, is implemented in the near wall regions of the domain, especially near the blade. About 4 elements are clustered near the proximity of the blade and 2 elements inside the boundary layer. This corresponds to about 25 grid points inside the boundary layer which is more than sufficient for resolving the boundary layer. Also, because of the distribution of quadrature points in GLL quadrature, the first node is placed very close to wall. A p-type refinement can be easily done without re-meshing and would enable higher resolution for flows at high Reynolds number. Also from a computational perspective, the solution can be restarted from a lower order run which enables considerable savings in time. The computed values of velocity are in the direction X,Y as shown in Fig. 28. They are converted to streamwise($\mathbf{t}$) and pitchwise($\mathbf{n}$) component of velocity by taking a dot product with the tangent and normal vector.

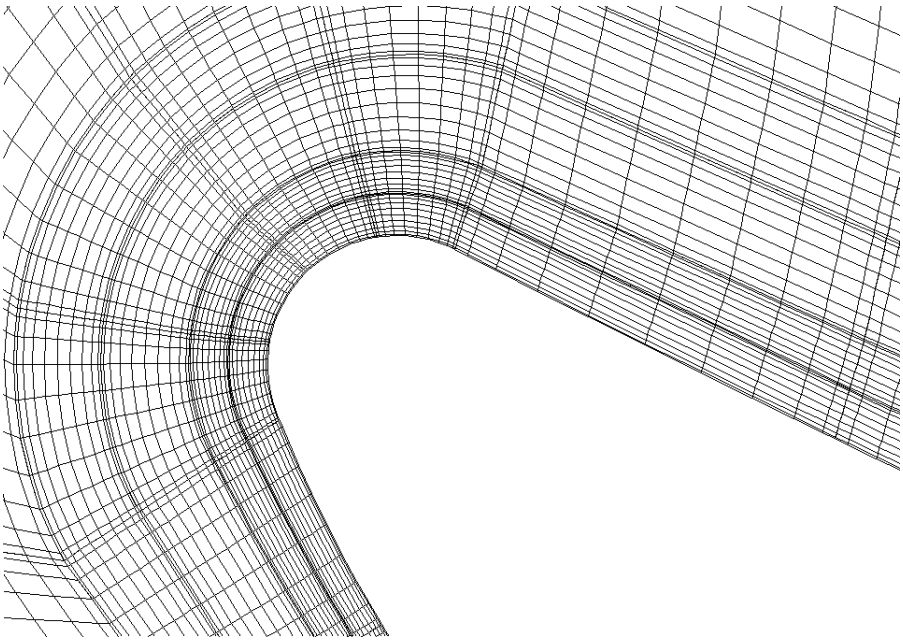

(a)

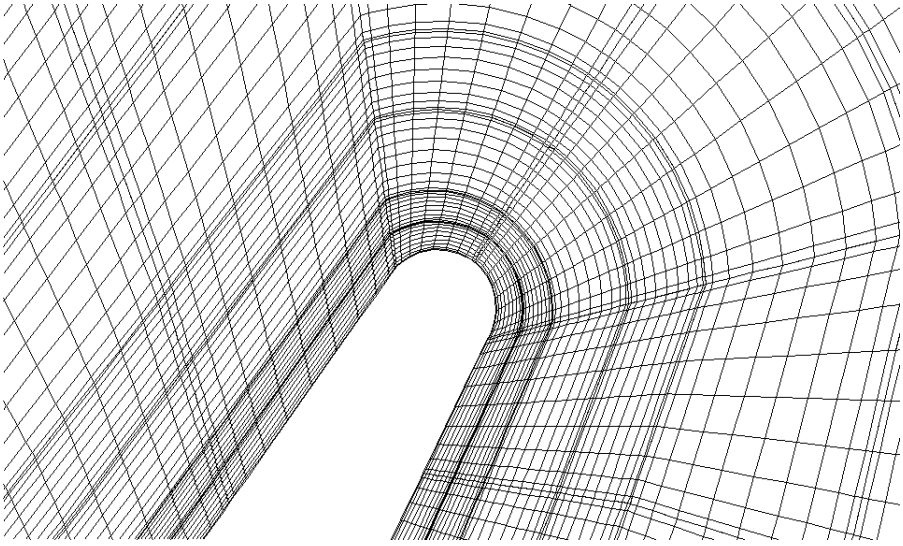

(b)

Fig. 27. (a) Leading and (b) Trailing edge mesh. A very fine mesh near the boundary layer is employed around the blade.

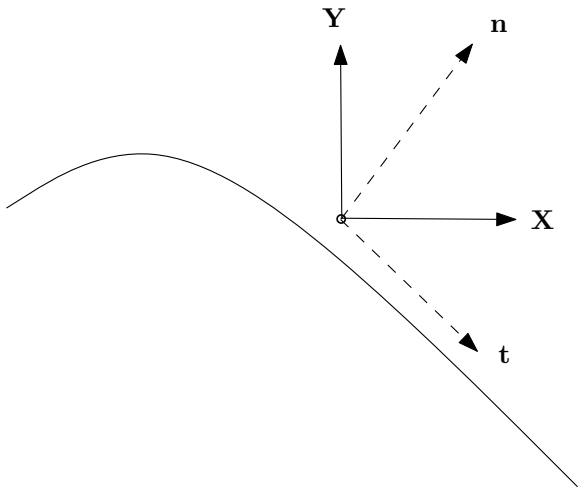

Fig. 28. The computed values of velocity are in the direction X and Y. They are converted to streamwise and pitchwise component of velocity by taking a dot product with the tangent and normal vector.

C. Results and Discussion

1. Pressure Distribution

The time and spatially averaged pressure distribution around the blade is shown in Fig. 29. The pressure distribution gives a fair description of the flow phenomenon around the blade indicating the regions of separation and transition and reattachment. However, for predicting the exact location of separation and reattachment, velocity profiles are visualized at different regimes of flow. The pressure side is subjected to very minimal adverse pressure gradient at the leading edge and hence a small separation and reattachment is seen. However, the suction side exhibits a different picture with highly accelerated flow till $s/s_o = 0.53$, where c_p reaches a minimum. Further downstream, the flow is dominated by the adverse pressure gradient that causes the boundary layer to separate, at $s/s_o = 0.61$. Since the flow is laminar prior to separation it is known as laminar separation bubble. The flow is laminar

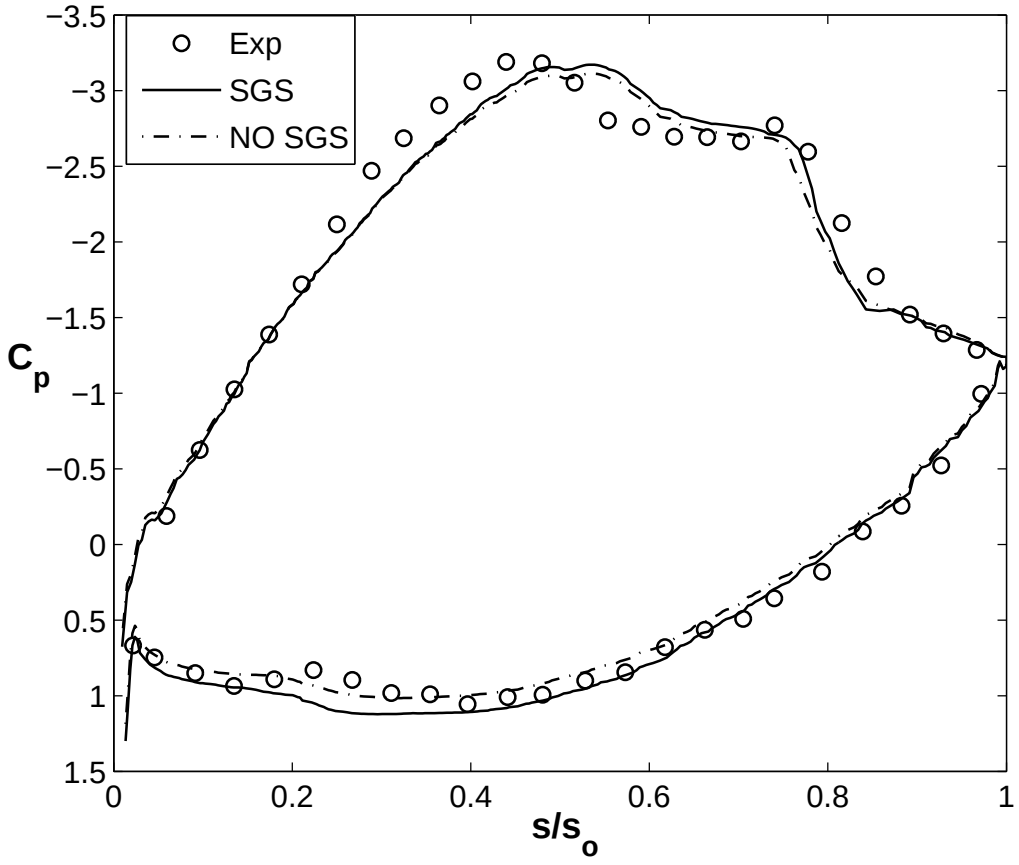

Fig. 29. The time and spanwise averaged pressure distribution around the blade is compared against the experiment with and without an SGS model. The onset of separation is at $s/s_o = 0.61$ and reattachment at $s/s_o = 0.81$. Minor separation and reattachment can be seen near the leading edge of the pressure surface. The onset of separation is illustrated by the constant cp regime. The experimental data is taken from Schobeiri et al. [8].

till $s/s_o = 0.75$ evidenced by a fairly constant pressure region, also known as dead air region. The separation bubble, in time mean sense, extends from $s/s_o = 0.61$ to $s/s_o = 0.81$ occupying about 20% of the suction surface. Experimentally, the bubble occupies 23% of the suction surface from $s/s_o = 0.55$ to $s/s_o = 0.78$. The computed pressure distribution is in excellent agreement with the experiment. Pressure side separation is observed and reported in both experiment and the simulations, however the shape and development of it is not investigated. The disparity in C_p on the pressure side can be due to the minor differences in the profile shape between the experiment and simulations. Near the leading edge, the pressure side profile displayed a small difference when compared to the actual profile. The suction side exhibits a reasonable agreement except near the separation and reattachment zones.

2. Statistical Quantities

The velocity distribution on the suction and pressure surface is essential to determine the growth of boundary layer upon separation and to fully understand the instability associated with the transition. Velocity profiles at six categorical locations is represented in Fig. 30. The boundary layer is laminar prior to separation. Upon separation the boundary layer begins to thicken and reaches a maximum at $s/s_o = 0.73$ and by $s/s_o = 0.81$ it reattaches to the surface.

The flow is attached and laminar until $s/s_o = 0.57$ as plotted in Fig. 30. An inflectional velocity profile can be seen at $s/s_o = 0.61$ which is marked as the start of separation. The separated but laminar boundary layer grows until $s/s_o = 0.73$ when boundary layer thickness is maximum. As will be shown later, the boundary layer becomes transitional after $s/s_o = 0.73$ and finally reattaches at $s/s_o = 0.81$ and remains turbulent thereafter. The velocity profiles shown in Fig. 31 compare the experiment and computed values along the suction side. The velocity profiles

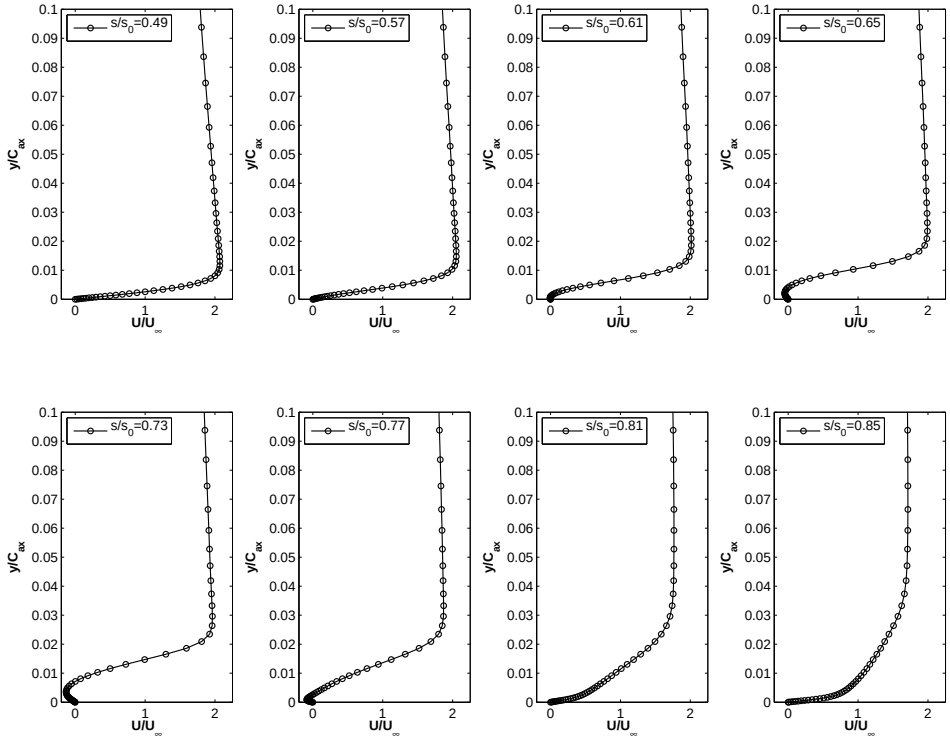

Fig. 30. Time mean streamwise velocity profiles on the suction surface. An inflectional velocity profile can be seen at $s/s_o = 0.61$ when the flow beings to separate. The boundary layer is laminar till $s/s_o = 0.73$, after which it becomes turbulent and reattaches at $s/s_o = 0.81$.

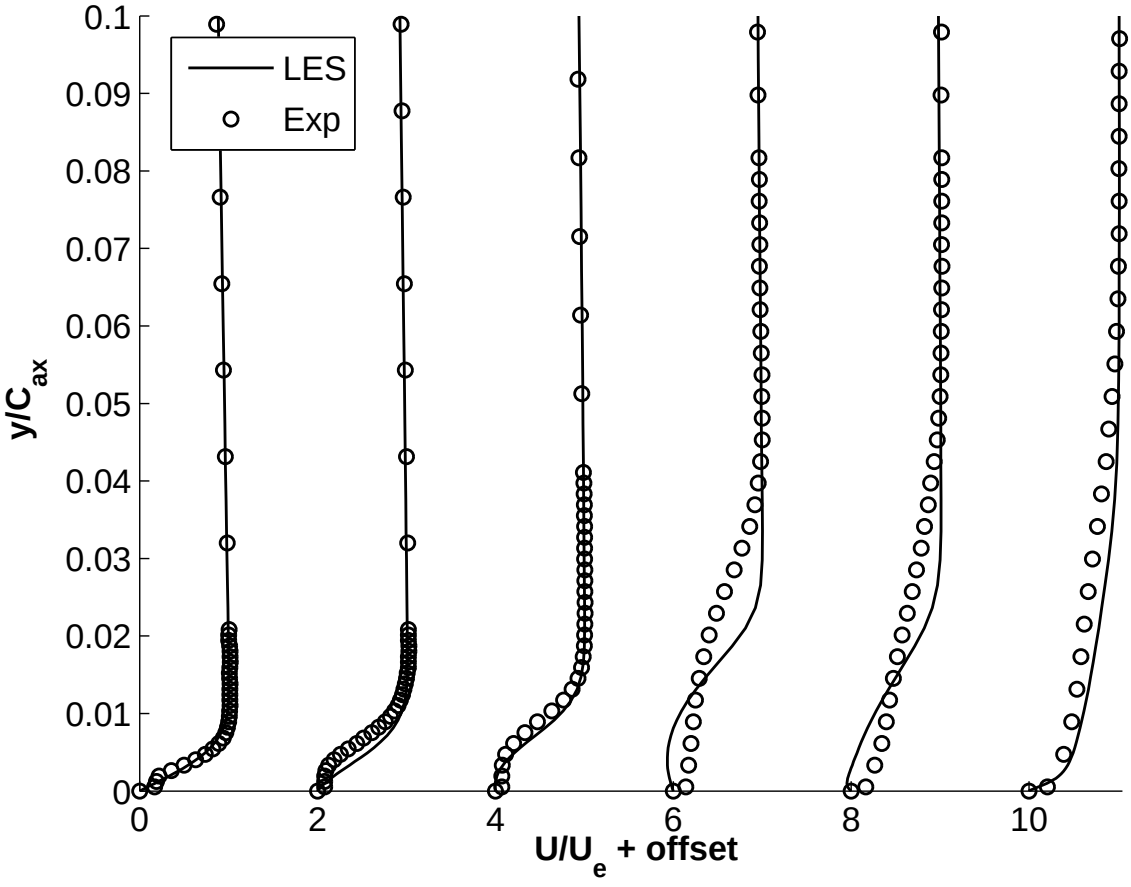

Fig. 31. Time mean streamwise velocity profiles on the suction side at $s/s_o = 0.49, 0.57, 0.61, 0.73, 0.77, 0.85$ from left to right. The velocity profiles are offset by 2.0 for clarity. The velocity profiles are in excellent agreement with the experiment of Schobeiri et al. [8] in the laminar flow regime until $s/s_o = 0.61$. Minor differences in the growth of boundary layer can be observed in the transitional regime at $s/s_o = 0.73, 0.75$.

follow the trend very well, and is in excellent agreement in the laminar regime. Minor differences can be seen in the transitional and turbulent regime where the LES under predicts the thickness of boundary layer. It is also to be noted that single wire probe does not recognize the direction of flow and the experimental data has not been mirrored in the plot. However, computationally the reverse velocities can be detected and plotted.

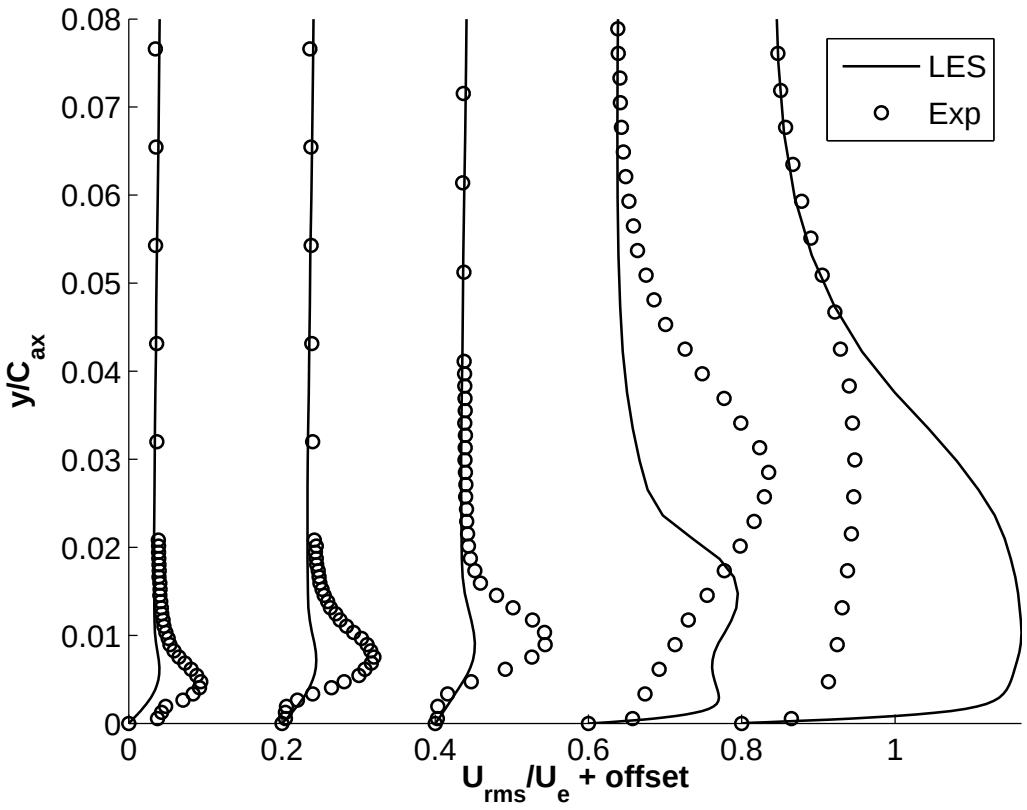

Fig. 32. Turbulence fluctuation rms at $s/s_o = 0.49, 0.57, 0.61, 0.73, 0.85$ from left to right. The profiles are offset by 0.2 in X-axis for clarity. The computed streamwise rms velocity follows the trend predicted by the experiment of Schobeiri et al. [8], but fails to comply with the experiment towards the turbulent flow regime at $s/s_o = 0.73, 0.85$.

The streamwise rms velocity profiles shown in Fig. 32 is in reasonable agreement with the experiment in the laminar regime but under-predicts the fluctuations inside the boundary layer. Also, in turbulent regime, LES over-predicts the rms. The turbulent flow regime is highly unsteady with spanwise oscillations more than 25% of the freestream velocity that makes makes experimental prediction with a single wire probe in the streamwise direction difficult and error-prone. The lack of an artificial viscosity in the LES model and insufficient dissipation from the stabilizing filter could also be a reason for the over-prediction.

The process of laminar-turbulent transition and reattachment occurs quickly and over a short streamwise distance because of the amplification of the instability. To further investigate the development of instability, the instantaneous velocity profiles is shown in Fig. 33.

At $y/l = 0.015$, the flow is inherently two-dimensional and steady until $s/s_o = 0.70$, when minor spanwise disturbance seem to occur. This disturbance propagates violently in the transitional regime reaching a maximum of about 20% of the freestream velocity. This localized growth of disturbance could be unstable in two ways, convectively unstable when the disturbance grows away from source and absolutely unstable if the disturbance spreads everywhere. Alam and Sandham [5] deduced a criterion for classifying the instabilities based on the reverse flow velocity inside the bubble. The threshold remains in the range of 15-20% of freestream velocity, but under LPT conditions the maximum observed reverse flow velocity as shown in Fig. 35(a) is less than 14% leads to the conclusion that the instability is convective in nature. Downstream of transition the pitchwise velocity increases dramatically showing signs of accelerated flow and thus reattachment. The ensuing minor oscillations in pitchwise velocity from $s/s_o = 0.875$ can be attributed to the vortex shedding from the bubble.

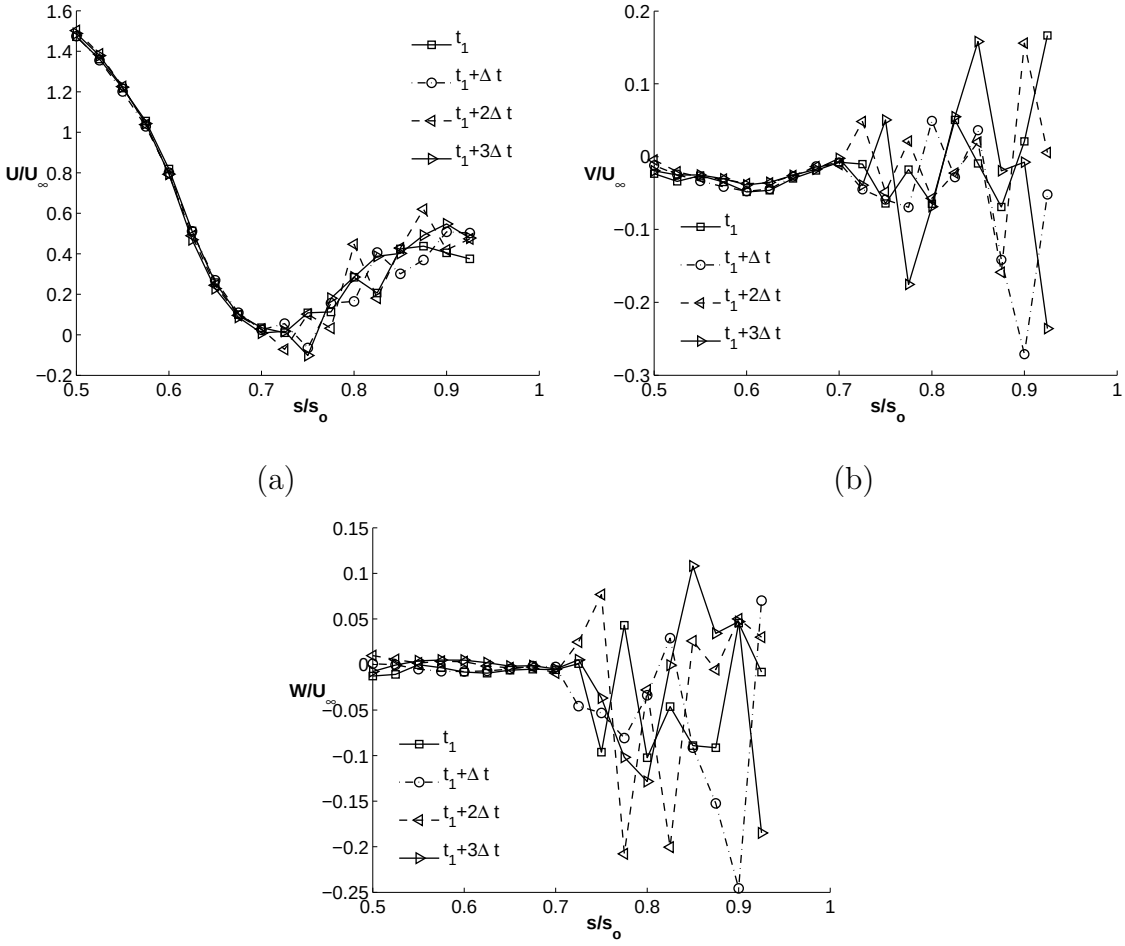

Fig. 33. Instantaneous velocity profiles at $y/l = 0.015$. The flow is nearly two-dimensional and steady until $s/s_o = 0.725$ where spanwise oscillations start. This instability grows and cause the transition to turbulence and reattachment.

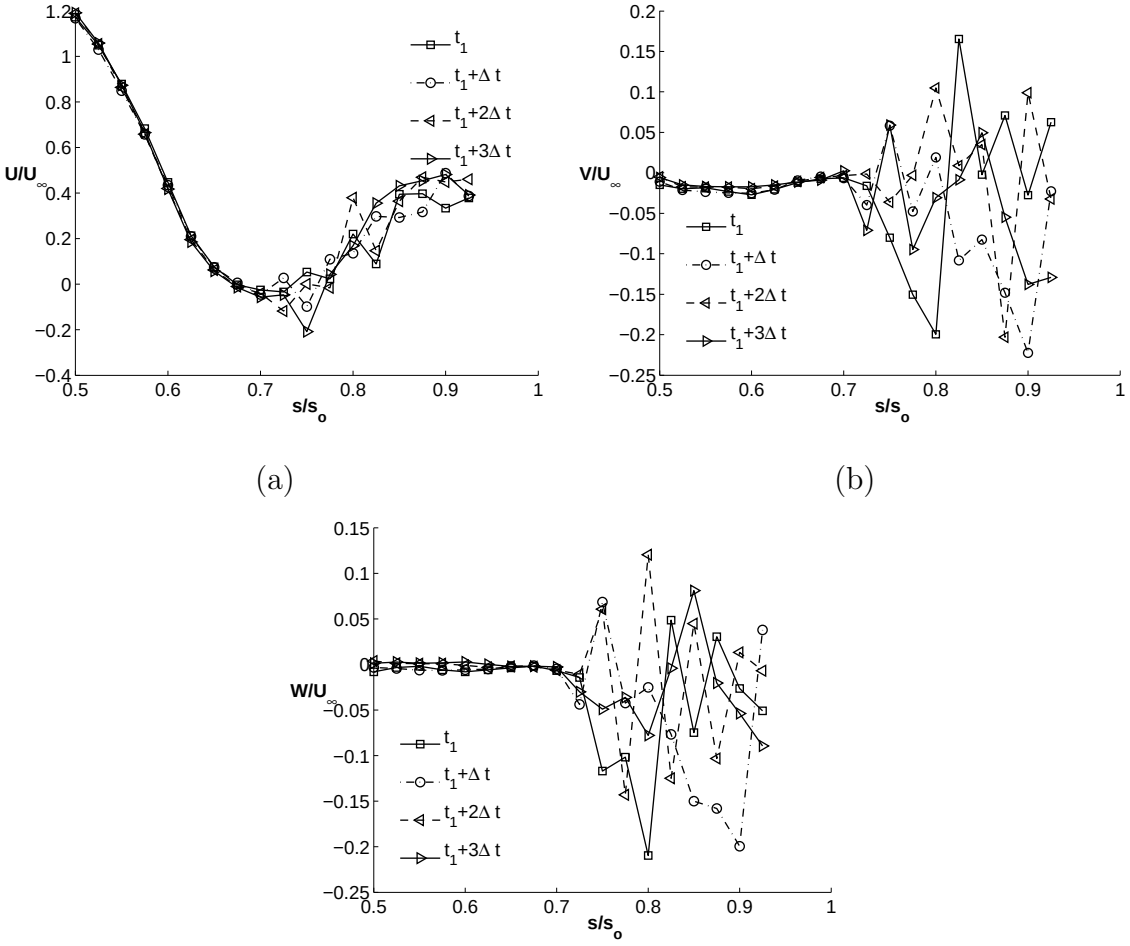

Fig. 34. Instantaneous velocity profiles at $y/l = 0.045$. The flow is not two dimensional. Minor spanwise starts to occur at $s/s_o = 0.725$ which propagates violently reaching a maximum of about 20% of freestream velocity.

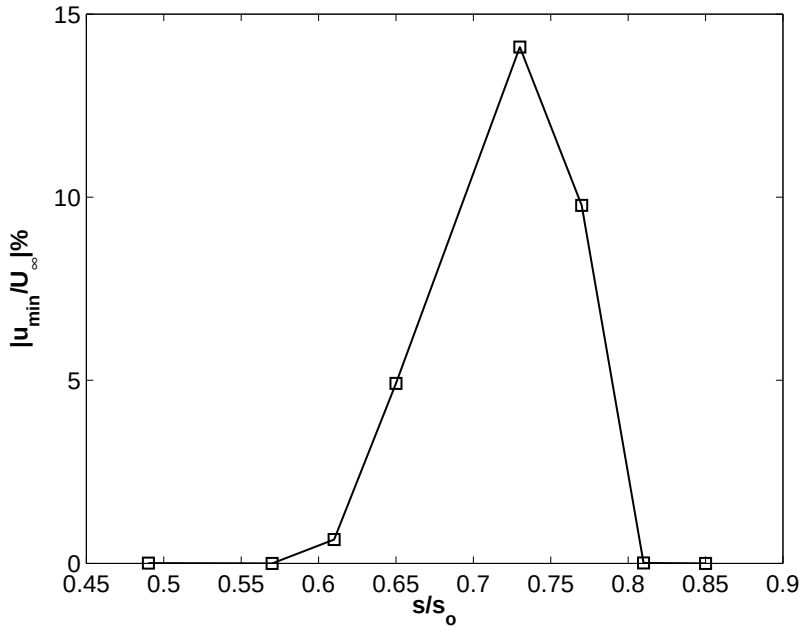

(a)

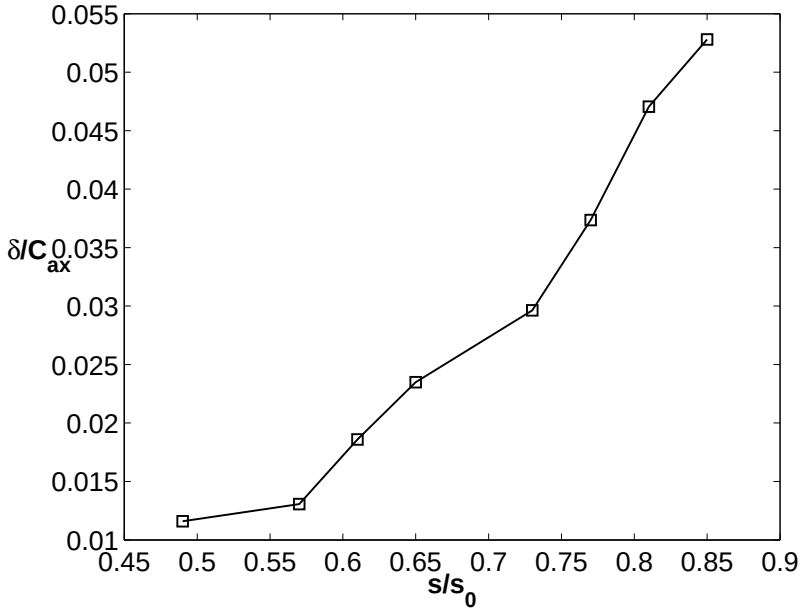

(b)

Fig. 35. (a)The maximum reverse flow velocity is less than 15% of the freestream velocity and the instability associated could be classified as convective according to Alam and Sandham [5]. (b) A distinct increase in the boundary layer thickness can be seen after $s/s_o = 0.73$.

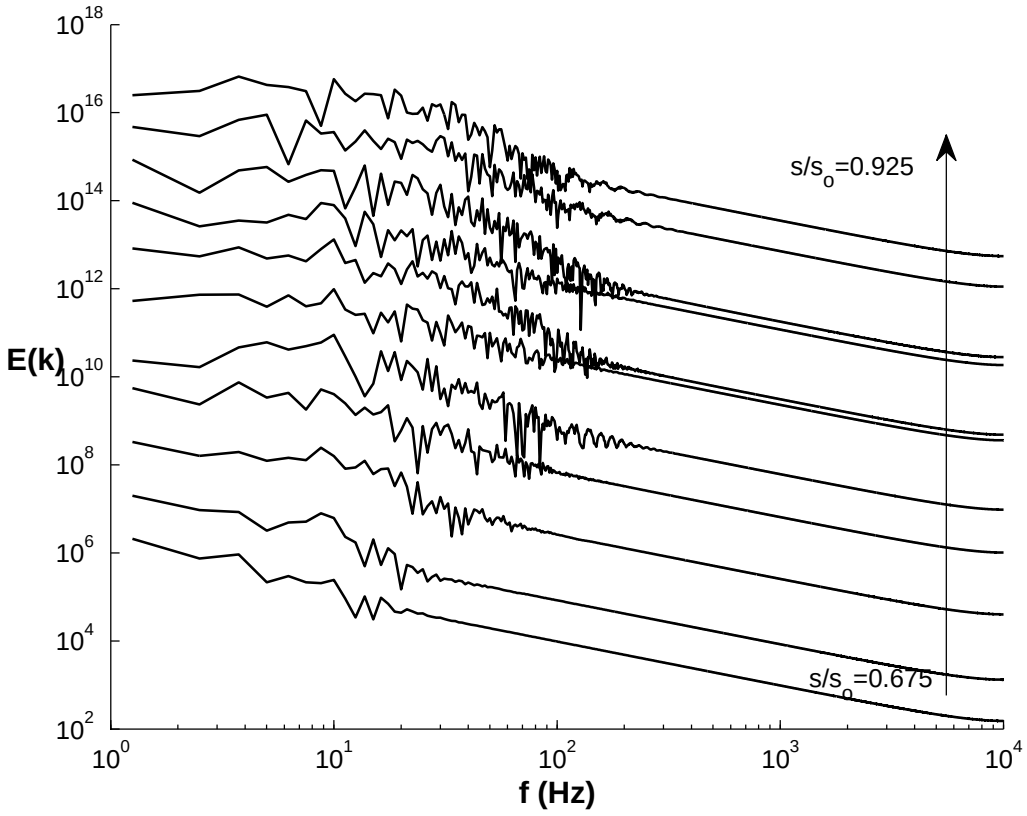

Fig. 36. Frequency spectra at different stream locations did not reveal a dominant frequency of oscillation. The Y-axis is offset in all the locations by 3 units for clarity.

The separated shear layer is approximately at a distance of $y/l = 0.045$ from the suction surface. Here, the flow is not two dimensional and spanwise oscillations, although minor, occur even in the laminar regime. The oscillations propagate violently at $s/s_o = 0.85$ reaching a maximum of over 20% of freestream velocity. This can be due to the unsteadiness associated with the reattachment. The Fourier transform of velocity signals shown in Fig. 36, however did not yield any dominant frequency range for the flapping.

3. Boundary Layer Parameters

Boundary layer parameters essential for characterizing the shape and growth of boundary layer are calculated. The average boundary layer edge velocity is calculated at different streamwise locations from which the displacement and momentum thickness are obtained from the following definitions [4],

$$\delta_1 = \int_0^\delta \left(1 - \frac{u}{U_e}\right) dy, \tag{3.1a}$$

$$\delta_2 = \int_0^\delta \frac{u}{U_e}\left(1 - \frac{u}{U_e}\right) dy. \tag{3.1b}$$

where δ is the boundary layer thickness and $u \simeq U_e$ at δ.

The displacement thickness,δ_1 shows a nominal increase in the laminar regime and reaches a maximum at $s/s_o = 0.725$ when breakdown to turbulence occurs. At this point there is enhanced mixing and entrainment from the free stream which reduces the boundary layer thickness but increases the momentum thickness, δ_2 as shown in Fig. 37(a). Near the trailing edge of the blade it decreases upon reattachment. The shape factor in Fig. 37(b) exhibits a very similar trend until transition, but declines sharply in the transitional regime of the flow. The variation of Reynolds number based on edge velocity and momentum thickness and variation of edge velocity shown in Fig. 38 confirms the point of trasition to be at $s/s_o = 0.725$.

4. Structure and Dynamics of flow

a. Suction Surface

The flow structures prior and aft-separation and time evolution of vortex structures are visualized using λ_2 criterion. Fig. 39 shows the spanwise vortices along the suction surface at different time instants. A minor spanwise disturbance sets in near $s/s_o =$

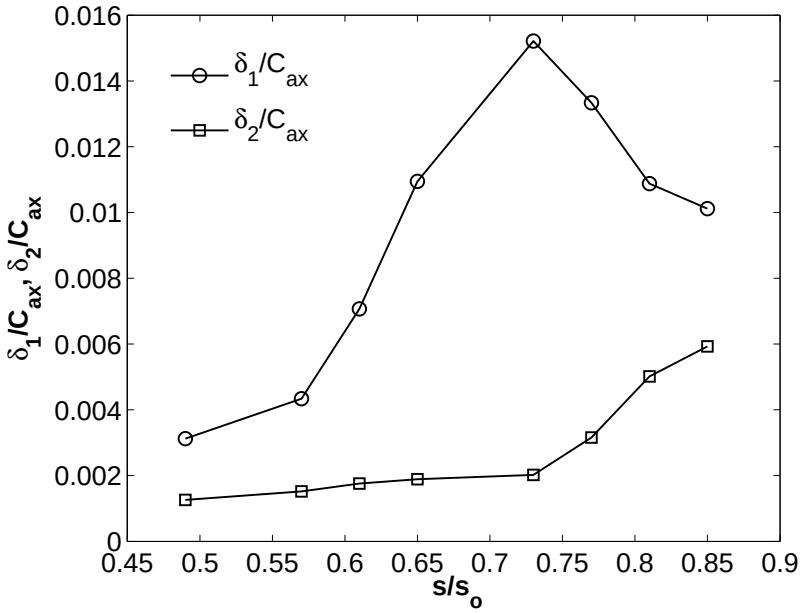

(a)

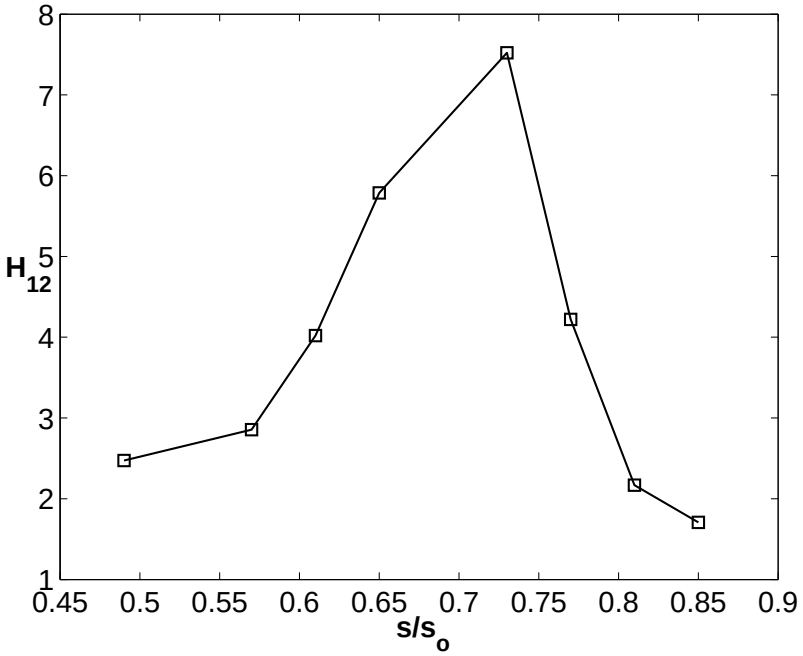

(b)

Fig. 37. (a) The displacement thickness is maximum at $s/s_o = 0.725$ and decreases further downstream which can be envisioned due to the transition to turbulence.(b) The form factor reduces after $s/s_o = 0.725$ which is typical of turbulent boundary layers.

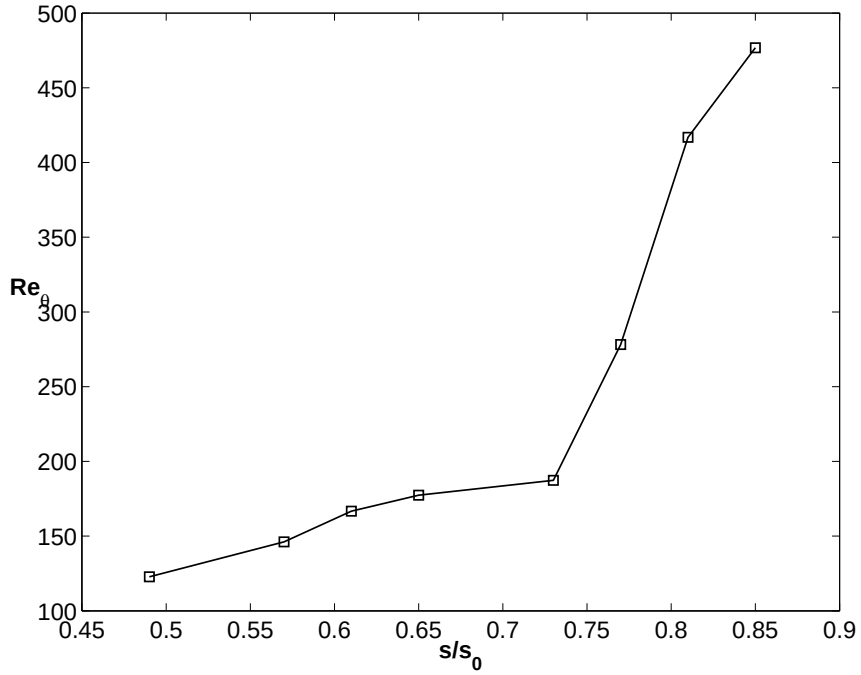

(a)

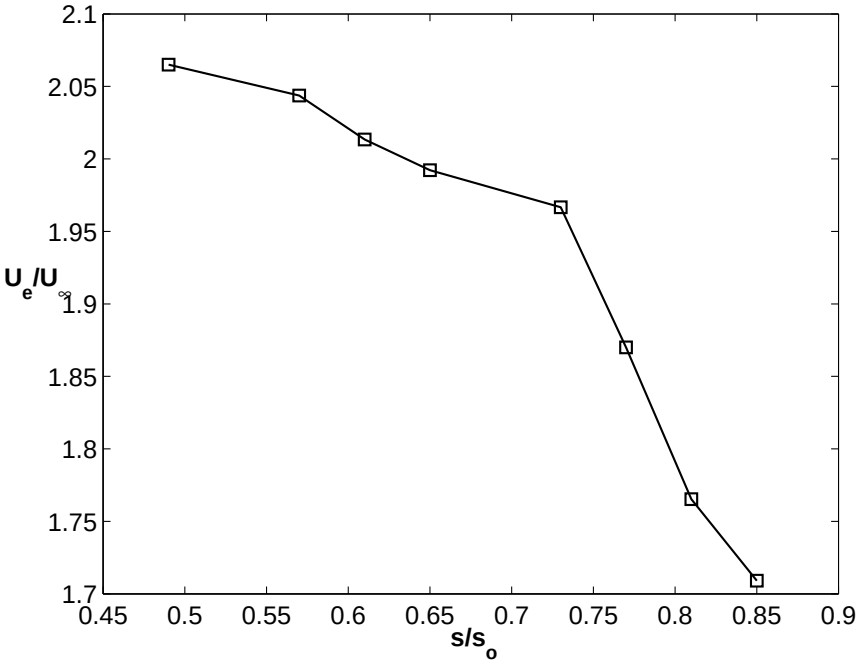

(b)

Fig. 38. (a) Re_θ is fairly constant till $s/s_o = 0.73$ but increases sharply in the turbulent regime (b) Boundary layer edge velocity distribution showing a sudden drop in U_e at the point of transition

0.725 that causes oscillatory motion of the separated shear layer Fig. 39(a).

The manifestation of this disturbance cause vortex shedding downstream that resemble the hairpin structure shown in Fig. 39(b). The legs of the vortex are engulfed in the velocity deficit regions of boundary layer while the tip of the vortex is accelerated by the freestream similar to the observations made by Acarlar and Smith [33]. As a result of this shear, the vortex is subjected to stretching and the hairpin structures become elongated and highly skewed. This is followed by the entrainment of freestream into the boundary layer causing an enhancement in mixing (Fig. 39(c)). The recirculation zone increases along the streamwise direction and a big vortical structure begin to evolve beneath the shear layer. The smaller vortical cores are shed downstream that impinge on the wall and interact with each other (Fig. 39(d)). As they move towards the trailing edge they migrate away from the wall and mix with the freestream increasing the turbulence intensity locally (Fig. 39(e) and (f)).

The separated shear layer can be clearly seen in Fig. 40(a) and (b). The vortices roll-up underneath the shear layer because of the entrainment from the freestream. The subsequent growth of the recirculation zone is evidenced from plots in Figs. 40(d)-(f). It is interesting to note that the observed separation bubble in Fig. 40 is identical to the classification described in Fig. 7 that consists of a dead-air zone and a recirculating vortex zone beneath the shear layer.

Fig. 41 shows the existence of several hairpin structures in the transitional and turbulent flow regime. The smaller and more pronounced vortex structures evolve at the beginning of transition, gets convected downstream by the external flow and evolve as bigger structures in the freestream. However, the structures seem to be convoluted. Downstream of the trailing edge, a big hairpin vortex can be clearly seen which signifies that hairpin structures are elongated but carried by the freestream.

The results are in conjunction with the findings of Alam and Sandham [5], Sarkar

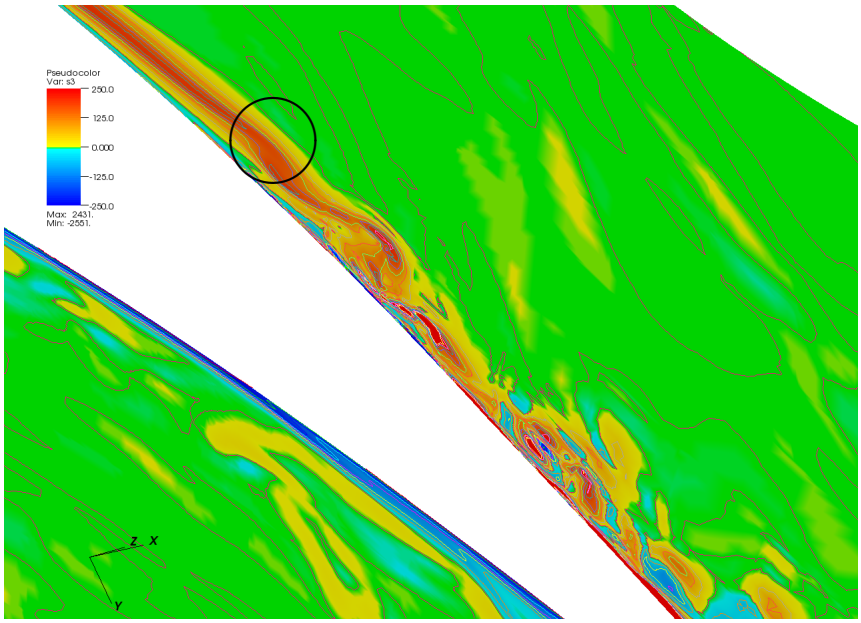

(a)

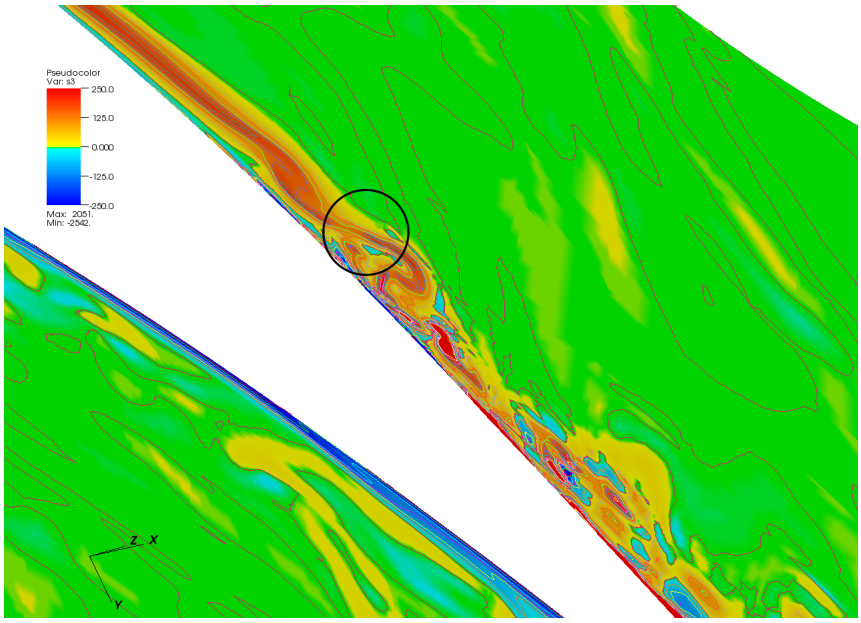

(b)

Fig. 39. Spanwise vorticity contours along the suction surface at different time instants. (a)- (c): The region of flapping of shear layer and ejection of vortices is shown with a circle. The separated shear layer is unstable and sheds vortices downstream that appear like hairpin structures. (d)- (f): The growth of recirculation region beneath the shear layer is evident.

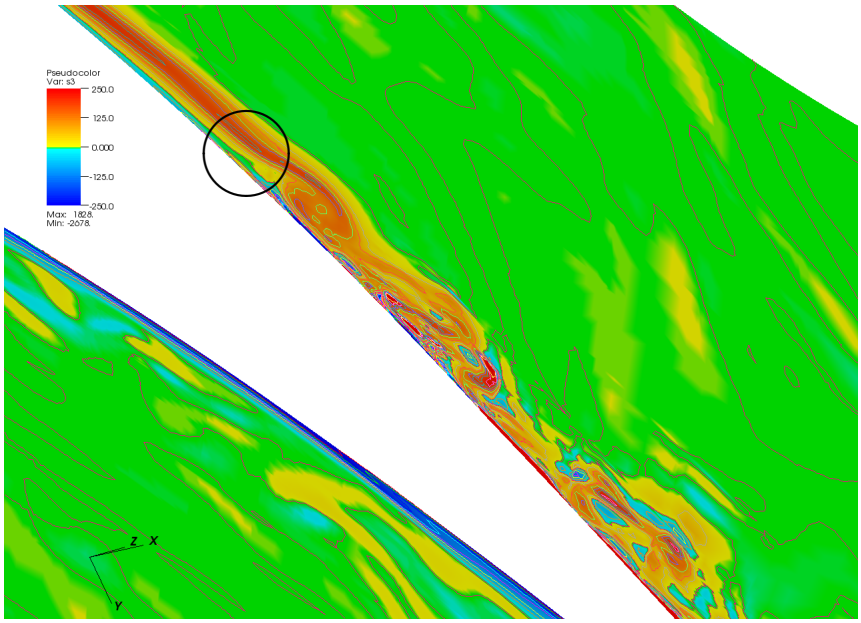

(c)

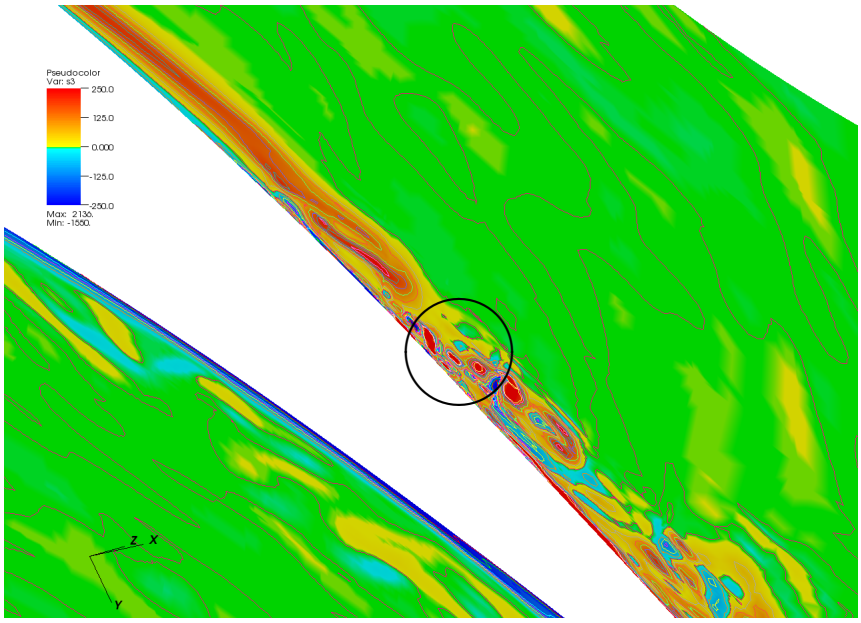

(d)

Fig. 39. Spanwise vorticity contours along the suction surface at different time instants. (a)- (c): The region of flapping of shear layer and ejection of vortices is shown with a circle. The separated shear layer is unstable and sheds vortices downstream that appear like hairpin structures. (d)- (f): The growth of recirculation region beneath the shear layer is evident (cont.)

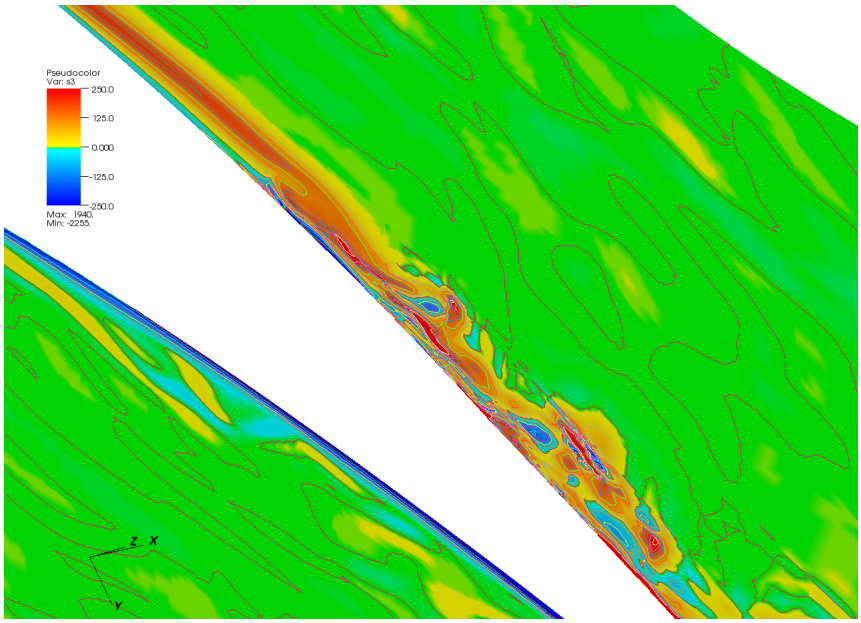

(e)

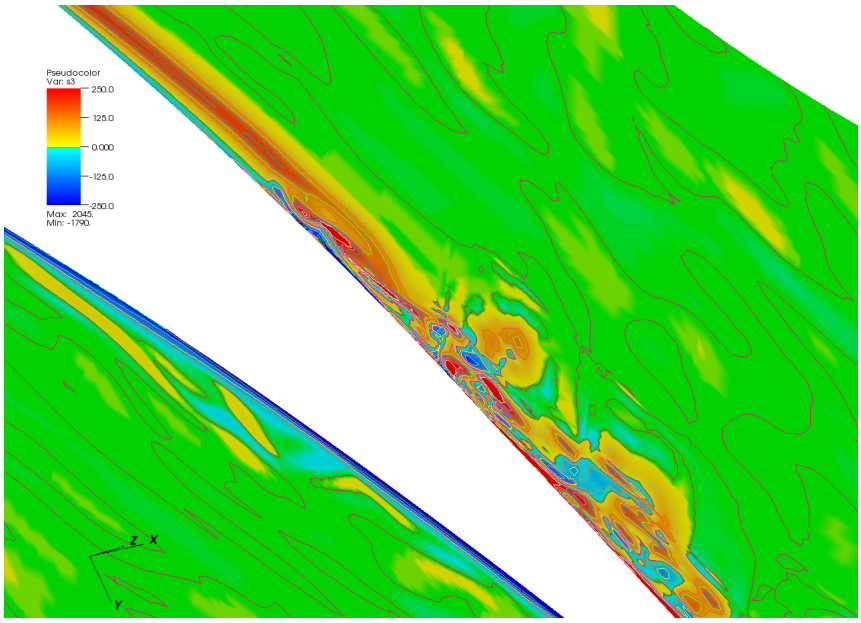

(f)

Fig. 39. Spanwise vorticity contours along the suction surface at different time instants. (a)- (c): The region of flapping of shear layer and ejection of vortices is shown with a circle. The separated shear layer is unstable and sheds vortices downstream that appear like hairpin structures. (d)- (f): The growth of recirculation region beneath the shear layer is evident.

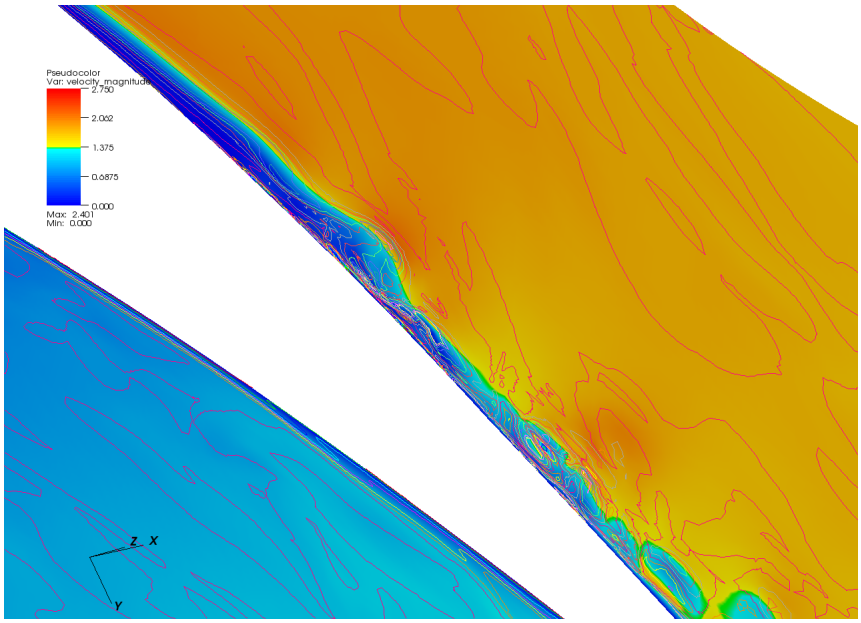

(a)

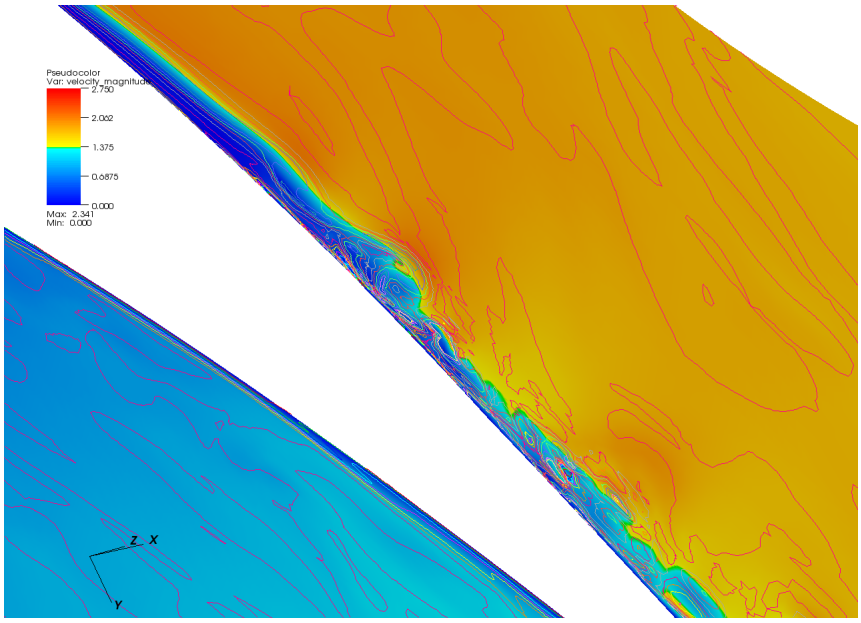

(b)

Fig. 40. Velocity contours near the suction surface boundary layer at different time instants superimposed on isolines of spanwise vorticity. (a)-(c): The flapping of separated shear layer and formation of roll-up vortex is clearly seen. (d)-(f): The shear layer is stabilized possibly by the growth of recirculation zone underneath.

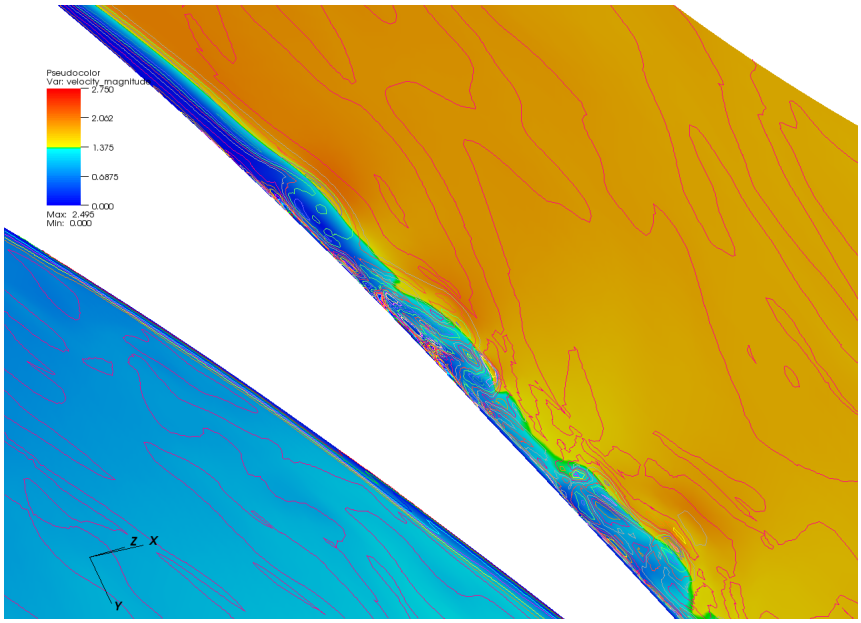

(c)

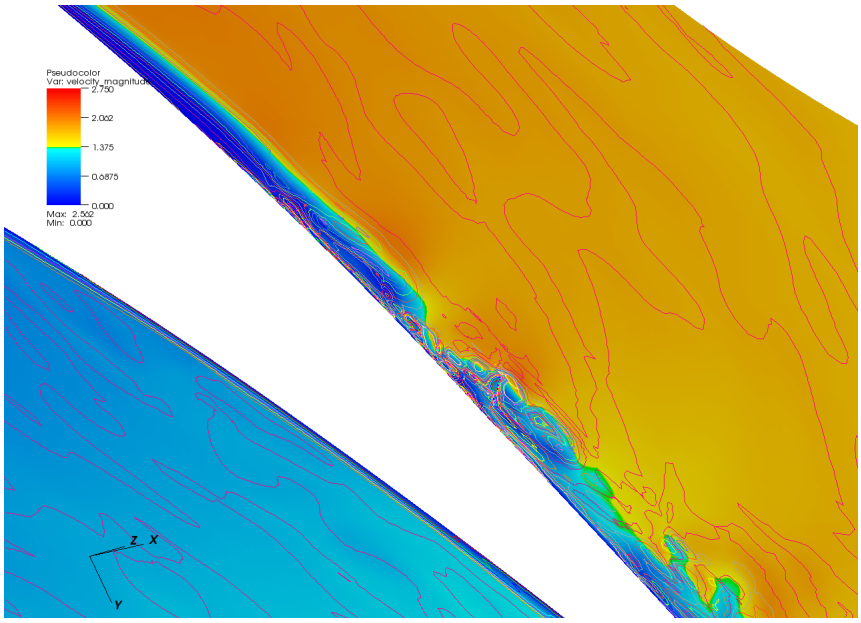

(d)

Fig. 40. Velocity contours near the suction surface boundary layer at different time instants superimposed on isolines of spanwise vorticity. (a)-(c): The flapping of separated shear layer and formation of roll-up vortex is clearly seen. (d)-(f): The shear layer is stabilized possibly by the growth of recirculation zone underneath (cont.).

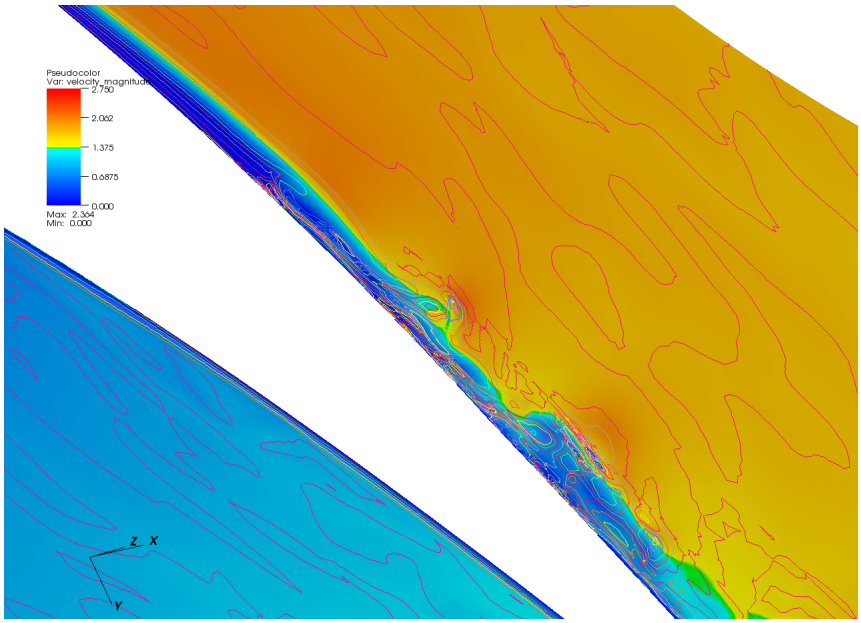

(e)

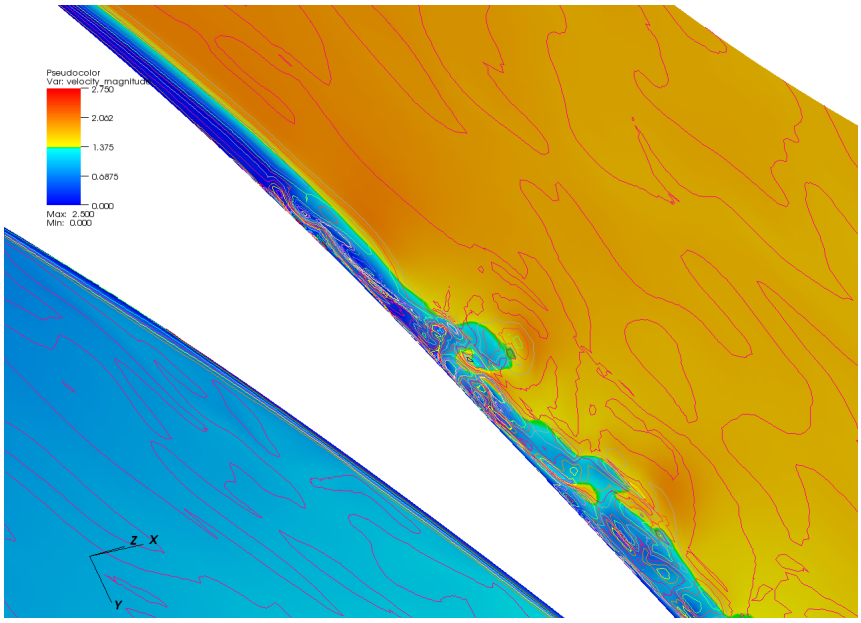

(f)

Fig. 40. Velocity contours near the suction surface boundary layer at different time instants superimposed on isolines of spanwise vorticity. (a)-(c): The flapping of separated shear layer and formation of roll-up vortex is clearly seen. (d)-(f): The shear layer is stabilized possibly by the growth of recirculation zone underneath.

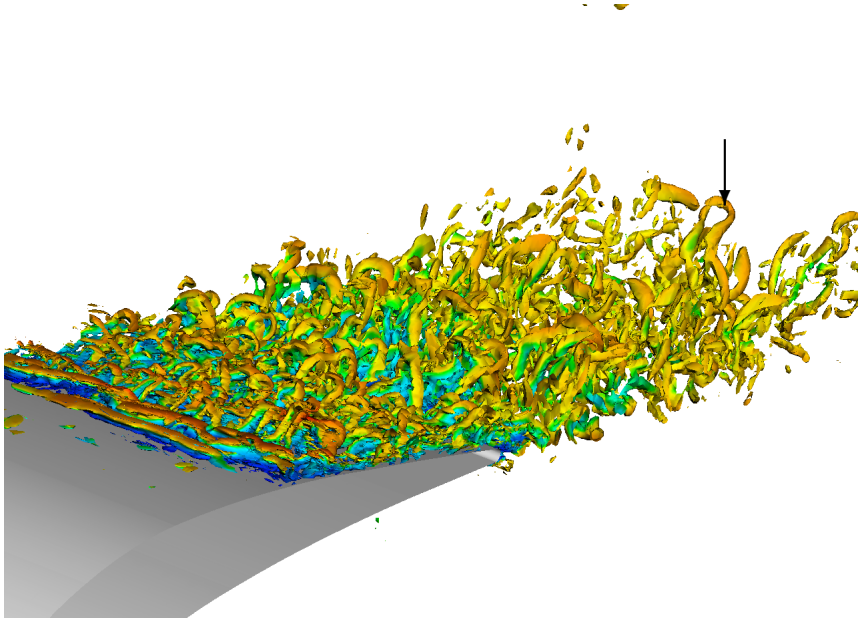

(a)

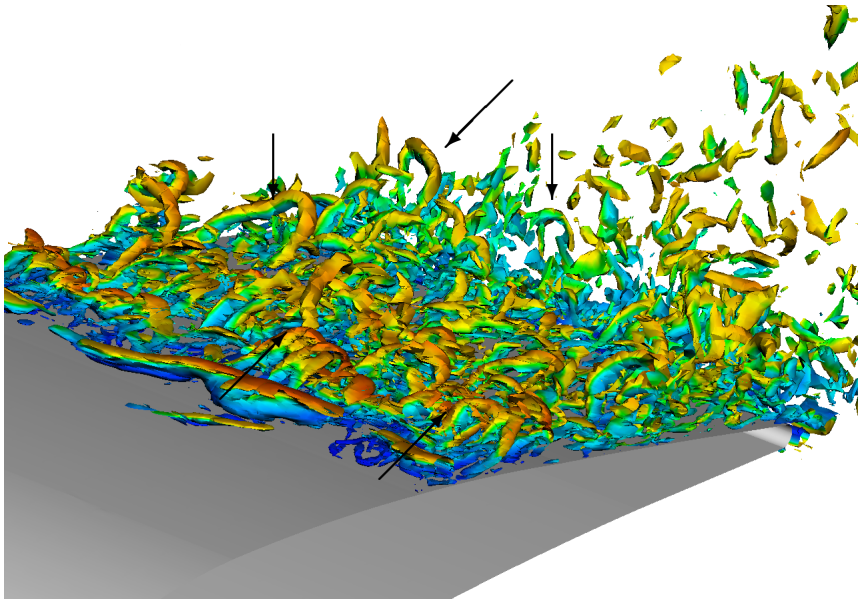

(b)

Fig. 41. (a) The arrow points to a hairpin vortex downstream of the trailing edge of the blade. (b) Smaller and dominant vortical structures of hairpin shape in the boundary layer are shown with arrows. Most of them are inclined to the surface and begin to evolve just downstream of the amplification of disturbance.

and Yoke [36] who also observed the the breakdown of Λ vortices and appearance of vortex legs as streaks.

b. Pressure Surface

Near the leading edge of the pressure surface, Λ vortices are formed, but since the flow accelerates, the structures don't persist for long. The head of Λ vortices splits into two distinct streamwise structures and is elongated by the freestream. It then appears as long streamwise structures near the trailing edge as shown in Fig. 42.

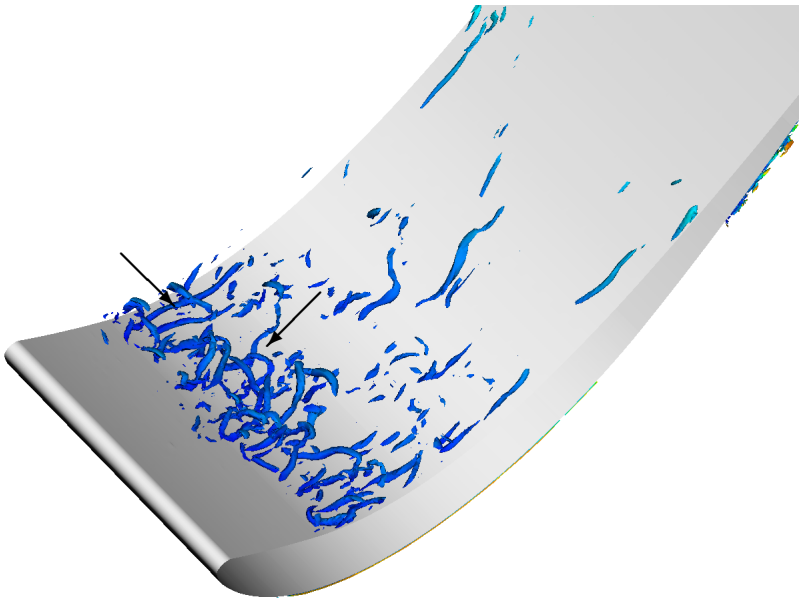

(a)

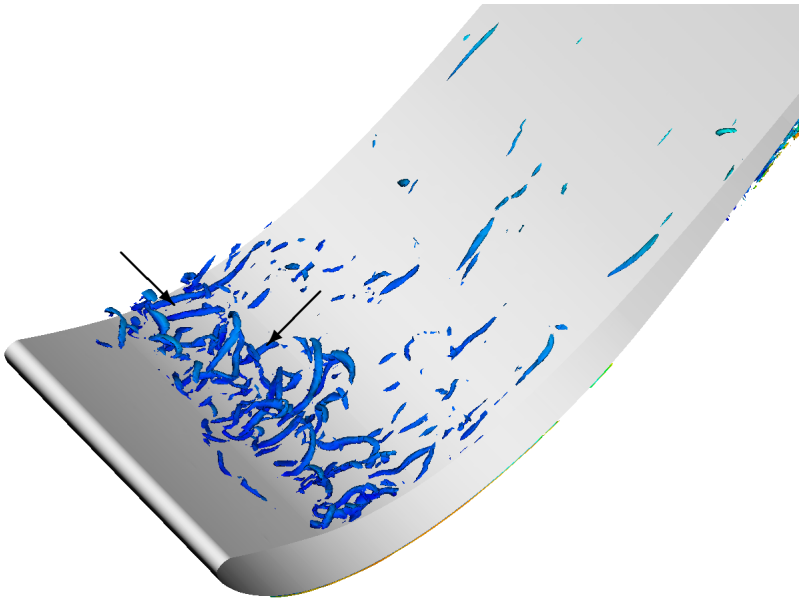

(b)

Fig. 42. (a) The arrows point to hairpin vortex structures near the leading edge of pressure surface. (b) Due to the flow acceleration, the head of hairpin vortex splits into distinct streamwise structures that gets elongated by the freestream. The arrow points to the horseshoe vortex that is split into two.

CHAPTER IV

CONCLUSIONS

The separation and reattachment of suction surface boundary layer is characterized using large eddy simulations. The high pass filtered Smagorinsky model is employed for modeling the sub-grid scales. On the suction side of the blade, at $s/s_o = 0.725$ minor spanwise disturbance start to occur. This instability propagates violently introducing an oscillatory motion of the shear layer that causes Λ vortices to shed downstream. The breakdown of these hairpin vortices is involved in the transition to turbulence and thus the reattachment. This is in conjunction with the findings of Roberts et al. [24] and Yang and Voke [22]. However, a dominant frequency for the shear layer flapping could not be determined from frequency spectra and a Proper Orthogonal Decomposition (POD) is suggested that would give more detail into the kinematics of the bubble. Dominant hairpin structures were observed close to the boundary layer and in the freestream after the trailing edge which shows that the effect of these vortices could be transported to the next stage. On the pressure surface, Λ vortices were observed near the leading edge, but due to the subsequent flow acceleration, the structures elongate evolving into streamwise streaks.

The pressure distribution on the suction side is in fair agreement with the experiment except near the separation and reattachment regime which may be attributed to the minor difference in inlet angle and turbulence intensity between the experiment and simulations. The streamwise extent of bubble is under-predicted by 3% as compared to the experiment. The pressure distribution follows the trend precisely as depicted by experiment. The velocity and rms profiles also show a fair comparison to the experiment.

REFERENCES

[1] Y. A. Cengel and J. M. Cimbala, *Fluid Mechanics: Fundamentals and Applications*. McGraw-Hill series in mechanical engineering, New York, NY: McGraw-Hill Higher Education, 2006.

[2] M. T. Schobeiri, *Turbomachinery Flow Physics And Dynamic Performance*. Heidelberg, New York: Springer Berlin, 2005.

[3] O. Reynolds, "An experimental investigation of the circumstances which determine whether the motion of water shall be direct or sinuous, and of the law of resistance in parallel channels.," *Philosophical Transactions of the Royal Society of London*, vol. 174, pp. 935–982, 1883.

[4] R. W. Fox, A. T. McDonald, and P. J. Pritchard, *Introduction to Fluid Mechanics*. Hoboken, New Jersey: Wiley, 2004.

[5] M. Alam and N. D. Sandham, "Direct Numerical Simulation of 'short' laminar separation bubbles with turbulent reattachment.," *Journal of Fluid Mechanics*, vol. 410, no. 4, pp. 1–28, 2000.

[6] P. K. Chang, "Separation of flow," *Journal of The Franklin Institute*, vol. 272, no. 6, pp. 433–448, 1961.

[7] H. P. Horton, *Laminar separation in two and three dimensional incompressible flow*. PhD thesis, University of London, 1968.

[8] M. T. Schobeiri, B. Ozturk, M. Kegalj, and D. Bensing, "On the physics of heat transfer and aerodynamic behavior of separated flow along a highly loaded low pressure turbine blade under periodic unsteady wake flow and varying of turbulence intensity," *Journal of Heat Transfer*, vol. 130, no. 5, 2008.

[9] L. F. Richardson, *Weather Prediction by Numerical Process*. Mineola, New York: Dover Publications, Inc., 1965 (Reprint of original 1922).

[10] S. B. Pope, *Turbulent Flows*. Trumpington Street, Cambridge: Cambridge University Press (U. K), 2000.

[11] M. T. Schobeiri, *Fluid Mechanics for Engineers: A Graduate Textbook*. Berlin, Heidelberg: Springer-Verlag, 2010.

[12] P. R. Owen and L. Klanfer, "On the Laminar Boundary Layer Separation from the leading edge of a thin aerofoil," *Aeronautical Research Council Technical Report*, no. C.P. No. 220 (16576), 1955.

[13] M. Gaster, "The structure and behaviour of separation bubbles," *Aeronautical Research Council Technical Report, Reports and Memoranda No. 3595*, March, 1967.

[14] H. P. Hodson and J. S. Addison, "Wake boundary layer interactions in an axial flow turbine rotor at off-design conditions," *Journal of Turbomachinery*, vol. 111, no. 2, pp. 181–192, 1989.

[15] L. Hilgenfeld, P. Stadtmller, and L. Fottner, "Experimental investigation of turbulence influence of wake passing on the boundary layer development of highly loaded turbine cascade blades," *Flow, Turbulence and Combustion*, vol. 69, pp. 229–247, 2002.

[16] W. R. Briley, "A numerical study of laminar separation bubbles using the Navier-Stokes equations," *Journal of Fluid Mechanics*, vol. 47, no. 04, pp. 713–736, 1971.

[17] M. M. O'Meara and T. J. Mueller, "Laminar separation bubble characteristics

on an airfoil at low Reynolds numbers.," *AIAA Journal*, vol. 25, no. 8, pp. 1033–1041, 1987.

[18] G. R. Inger, "A theoretical study of spanwise-periodic 3-D disturbances in the wake of a slightly stalled wing at low Reynolds numbers," *Proceedings of the International Conference, London, England*, pp. 4.1–4.21, 1986.

[19] G. Kalitzin, X. H. Wu, and P. A. Durbin, "DNS of fully turbulent flow in a LPT passage," *International Journal of Heat and Fluid Flow*, vol. 24, no. 4, pp. 636–644, 2003.

[20] J. Wissink and W. Rodi, "LES of background fluctuations interacting with periodically incoming wakes in a turbine cascade," in *Direct and Large-Eddy Simulation VI* (E. Lamballais, R. Friedrich, B. Geurts, and O. Métais, eds.), pp. 609–616, Springer Netherlands, 2006.

[21] V. Michelassi, J. G. Wissink, J. Frohlich, and W. Rodi, "Large-Eddy Simulation of flow around low-pressure turbine blade with incoming wakes," *AIAA Journal*, vol. 41, no. 11, pp. 2143–2156, 2003.

[22] Z. Yang and P. R. Voke, "Large-Eddy Simulation of boundary-layer separation and transition at a change of surface curvature," *Journal of Fluid Mechanics*, vol. 439, no. -1, pp. 305–333, 2001.

[23] B. R. McAuliffe and M. I. Yaras, "Transition mechanisms in separation bubbles under low- and elevated-freestream turbulence," *Journal of Turbomachinery*, vol. 132, no. 1, 2010.

[24] S. K. Roberts and M. I. Yaras, "Large-Eddy Simulation of transition in a separation bubble," *Journal of Fluids Engineering*, vol. 128, no. 2, 2006.

[25] P. G. Wilson and L. L. Pauley, "Two- and three-dimensional large-eddy simulations of a transitional separation bubble," *Physics of Fluids*, vol. 10, no. 11, pp. 2932–2940, 1998.

[26] H. P. Horton, "A semi-empirical theory for the growth and bursting of laminar separation bubbles," *Aeronautical Research Council*, 1969.

[27] X. Wu and P. A. Durbin, "Boundary layer transition induced by periodic wakes," *Journal of Turbomachinery*, vol. 122, no. 3, pp. 442–449, 2000.

[28] P. Sagaut, *Large Eddy Simulation for Incompressible Flows: An Introduction*. Berlin, Heidelberg: Springer-Verlag, 2006.

[29] P. Schlatter, S. Stolz, and L. Kleiser, "LES of transitional flows using the Approximate Deconvolution Model," *International Journal of Heat and Fluid Flow*, vol. 25, no. 3, pp. 549 – 558, 2004. Turbulence and Shear Flow Phenomena (TSFP-3).

[30] A. Leonard, "Energy cascade in Large-Eddy Simulations of turbulent fluid flows," *Adv in Geophys. A*, vol. 18, pp. 237–248, 1974.

[31] P. F. Fischer, G. W. Kruse, and F. Loth, "Spectral Element Methods for transitional flows in complex geometries," *J. Sci. Comput.*, vol. 17, no. 1-4, pp. 81–98, 2002.

[32] S. Stolz and N. A. Adams, "Large-Eddy Simulation of high-reynolds-number supersonic boundary layers using the approximate deconvolution model and a rescaling and recycling technique," *Physics of Fluids*, vol. 15, no. 8, pp. 2398–2412, 2003.

[33] M. S. Acarlar and C. R. Smith, "A study of hairpin vortices in a laminar boundary layer. Part 1. Hairpin vortices generated by a hemisphere protuberance," *Journal of Fluid Mechanics*, vol. 175, no. -1, pp. 1–41, 1987.

[34] J. Jeong and F. Hussain, "On the identification of a vortex," *Journal of Fluid Mechanics*, vol. 285, no. -1, pp. 69–94, 1995.

[35] L. C. Berselli, T. Iliescu, and W. J. Layton, *Mathematics of Large Eddy Simulation of Turbulent Flows*. Berlin, Heidelberg: Springer-Verlag, 2005.

[36] S. Sarkar and P. R. Voke, "Large-Eddy Simulation of unsteady surface pressure over a low-pressure turbine blade due to interactions of passing wakes and inflexional boundary layer," *Journal of Turbomachinery*, vol. 128, no. 2, pp. 221–231, 2006.

VITA

Shriram Jagannathan was born in India in the year 1987. After completing his Bachelor of Technology at National Institute of Technology, Tiruchirappalli, he began his Master's program at Texas A&M University in Fall 2008. Since then, he has been working with the Fluids, Turbulence and Fundamental Transport Lab (FT^2L) under the supervision of Dr. Andrew Duggleby. He graduated in December 2010.

He can be reached at:

Mechanical Engineering Department,
c/o Dr. Andrew Duggleby
Texas A&M University
College Station, TX 77843-3123.

The typist for this thesis was the author.